Computational Modeling and Experimental Characterization of Pneumatically Driven Actuators for the Development of a Soft Robotic Arm

by

Sai Gautham Nuthi

A Thesis Presented in Partial Fulfillment
of the Requirements for the Degree
Master of Science

Approved April 2018 by the
Graduate Supervisory Committee:

Panagiotis Polygerinos, Chair
Hyunglae Lee
Sze Zheng Yong

ARIZONA STATE UNIVERSITY

May 2018

ABSTRACT

Soft Poly-Limb (SPL) is a pneumatically driven, wearable, soft continuum robotic arm designed to aid humans with medical conditions, such as cerebral palsy, paraplegia, cervical spondylotic myelopathy, perform activities of daily living. To support user's tasks, the SPL acts as an additional limb extending from the human body which can be controlled to perform safe and compliant mobile manipulation in three-dimensional space. The SPL is inspired by invertebrate limbs, such as the elephant trunk and the arms of the octopus. In this work, various geometrical and physical parameters of the SPL are identified, and behavior of the actuators that comprise it are studied by varying their parameters through novel quasi-static computational models. As a result, this study provides a set of engineering design rules to create soft actuators for continuum soft robotic arms by understanding how varying parameters affect the actuator's motion as a function of the input pressure. A prototype of the SPL is fabricated to analyze the accuracy of these computational models by performing linear expansion, bending and arbitrary pose tests. Furthermore, combinations of the parameters based on the application of the SPL are determined to affect the weight, payload capacity, and stiffness of the arm. Experimental results demonstrate the accuracy of the proposed computational models and help in understanding the behavior of soft compliant actuators. Finally, based on the set functional requirements for the assistance of impaired users, results show the effectiveness of the SPL in performing tasks for activities of daily living.

TABLE OF CONTENTS

Page

CHAPTER

CHAPTER Page

APPENDIX

LIST OF TABLES

Table Page

LIST OF FIGURES

Figure Page

PREFACE

The following thesis is the work I have done for the development of computational models of soft robotic actuators and optimization of their design parameters by experimental characterization. I worked on this project in the Bio-Inspired Mechatronic Laboratory at Arizona State University, for more than a year and co-authored a research paper (Pham Huy Nguyen et al. 2018), which was sent for review to Science Robotics for publication. I grant permission for all my co-authors of the research paper to reuse any of the content from this thesis.

I would like to express my gratitude to Dr. Panagiotis Polygerinos for his constant support and encouragement. I would also like to thank all the doctoral students at Bio-Inspired Mechatronics lab for their advice and support. To my friends and family, thank you for your encouragement and support throughout my studies.

CHAPTER 1

INTRODUCTION

Cervical Spondylotic Myelopathy is a degenerative condition affecting limb function (Lubelski et al., 2016), Cerebral Palsy is a group of neurological disorders that permanently affect body movement and muscle co-ordination (Kirby et al., 2011), Paraplegia is paralysis of both legs and lower part of the body, resulting from injury to the spinal cord at the level of lower back or level of the chest, Quadriplegia is paralysis of both arms and legs resulting from injury involving the spinal cord at the level of neck. All these medical conditions result in difficulties in performing activities of daily living (Ajiboye et al., 2017), such as picking up a cup, grasping an object, and other similar tasks.

***Figure 1**: Conceptual soft robotic arm assisting an impaired user.*

To aid this population to perform activities of daily living tasks, a soft wearable continuum arm is designed. This thesis presents, a set of design rules for creating the soft robotic arm, named Soft Poly-Limb (SPL). Fig.1 shows a conceptual soft robotic arm which assists the user in lifting a cup to drink.

Soft robotic arms are fabricated using highly compliant soft materials, which makes it easy to conform to the obstacles and carry fragile objects, unlike traditional hard hyper-redundant robotic arms. Traditional rigid robotic arms have multiple joints connected by stiff links. Each joint has one degree of freedom either in translational or rotational direction. The workspace of these robotic arms is defined by the locus of points the tip position of the arm can achieve. These arms are mostly kinematically redundant and are used in performing repetitive tasks very accurately in a well-defined environment. Soft robotic arms unlike traditional rigid robotic arms have distributed deformation. These arms have an infinite number of degrees of freedom, leading to hyper-redundancy. These arms can reach to every position in the three-dimensional workspace. The joint positions of a rigid robotic arms can be processed by the forward kinematics to determine the position and orientation of the end effector, similarly the joint angles can be determined by performing inverse kinematics when the desired position is provided, but in case of soft robotics arms as there are no pre-determined joints and links, and they have distributed deformation, which makes these traditional methods inapplicable.

Traditional robotic manipulators are designed to be stiff so that vibration and deformation of the structure, do not reduce the accuracy and movement (Trivedi, Rahn, Kier, & Walker, 2008). This type of design aspects makes the traditional robot heavy and unsafe to interact with people without causing injuries. Whereas, the high compliant nature and their lightweight makes the soft robotic arms ideal to interact with people.

The purpose of this thesis is to identify various geometrical and physical parameters involved in fabricating actuators of the SPL and study their effect as a function of pressure. To study the actuator's motion and behavior at different pressures and loading conditions, computational modeling methods are employed which aim at producing novel models that allow rapid variation of their individual parameters. Computational modeling of such type of non-linearly behaving actuators expedites the research process by optimizing their performance without the cost of having to fabricate and characterize physical prototypes.

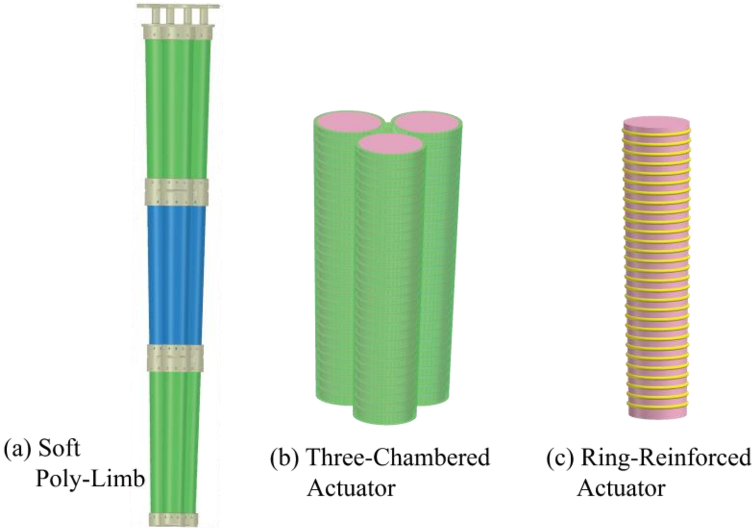

Figure 2: *Soft Poly-Limb and its components.*

The main components of the SPL (figure 2(a)) are the three-chambered actuators and the ring-reinforced actuators. Ring-Reinforced actuator (RRA) (figure 2(c)) is a novel elastomeric actuator which consists of an inner elastomeric tube reinforced with rings. Three-Chambered Actuator (3CA) is formed by bundling three RRAs together in a parallel formation.

This thesis comprises of material characterization, a detailed computational study on RRA, 3CA and SPL, and a discussion on future work. In particular, chapter 2 describes the biological inspiration for the development of soft robotics arm, prior work on soft robotic actuators and soft robotic arms. Chapter 3 is focused on characterizing the hyperelastic silicone rubbers with shore hardness 10A, 20A and 30 A. Uniaxial tensile strength test is conducted on these materials as per ASTM D638-02a standards and the data obtained is curve fitted with various hyperelastic models to obtain material coefficients for computational modeling. Chapter 4 describes the various design requirements for the development of the arm. Chapter 5 describes various geometrical and physical parameters of the RRA. Computation modeling performed to understand the effect of variation of each parameter and fabrication process of the RRA. To evaluate the accuracy of the computational model linear expansion test is performed and to study the operational life of these actuators fatigue test is performed. Chapter 6 describes the parameters of 3CA, computational modeling performed by varying the parameters to understand the behavior of the 3CA, Fabrication process of the 3CA, bending angle test performed to study the accuracy of the computation model is also explained. Chapter 7 explains the accuracy of the computational model of the arm by performing an arbitrary pose test. Chapter 8 summarizes the contributions of this thesis and discusses the future work.

CHAPTER 2

BACKGROUND

Biological Inspiration

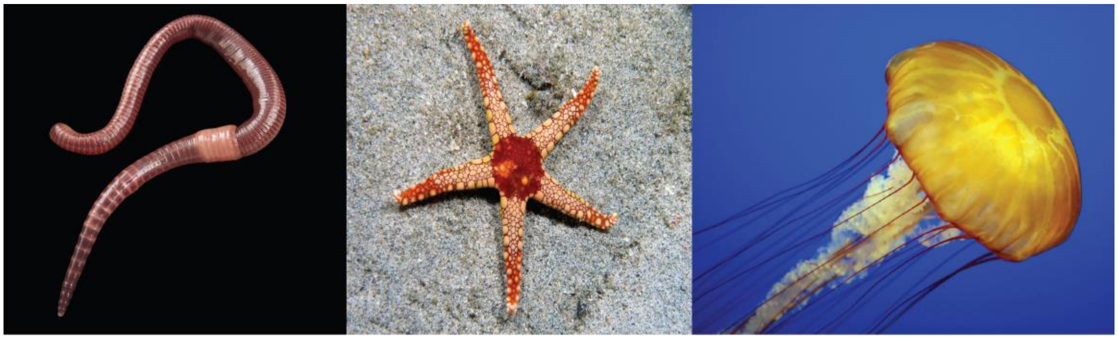

(a) Earthworm
(JOEL SARTORE, NATIONAL GEOGRAPHIC PHOTO)

(b) Starfish
(N NICK HOBGOOD, WIKIPEDIA COMMONS)

(c) Jellyfish
(DAN, WIKIPEDIA COMMONS)

***Figure 3**: Animals with fluid-filled, hydrostatic skeletons.*

Invertebrates such as arthropod, mollusk, worms, etc., do not have a vertebral column. Some of these animals like earthworms (figure 3(a)), starfish (figure 3(b)), jellyfish (figure 3(c)), etc., have fluid-filled, hydrostatic skeletons. Hydrostatic skeletons are long cylindrical fluid-filled cavities surrounded by a muscular wall that is reinforced with connective tissue fibers (Trivedi et al., 2008). Contractions of the circular muscles increase the length of the organism’s body and contractions of the longitudinal muscles decrease the size of the organism’s body. The fluid in these skeletons is often water, and it allows these organisms to move around easily, but if they expand their body too much they would collapse under their own weight.

(a) Trunk of an Elephant (b) Arms and Tentacles of a Squid

(GODUTCHBABY, FLICKR) (HANS HILLEWAERT, WIKIPEDIA COMMONS)

(c) Tongue of a Dog (d) Arm of an Octopus

(ELDADCARIN, GETTY IMAGES) (STAFF,WWW.LIVESCIENCE.COM)

Figure 4*: Animals with muscular hydrostats.*

Trunk of an Elephant (figure 4(a)), arms and tentacles of a squid (figure 4(c)), tongue of a dog (figure 4(c)), arms of an octopus (figure 4(d)), are a type of invertebrate structures which consists mainly muscles with no skeletal support. These structures are termed as "muscular hydrostats" and assist the animals to manipulate items. Their compliant motion is due to the arrangement of the muscles which generates force for the movement and also acts as a skeleton to offer support. The biomechanics and the abilities demonstrated by these muscular hydrostats (KIER & SMITH, 1985), such as elephant trunks, octopus arms and squid tentacles have inspired research activity in soft continuum robots.

Soft Robotic Actuators

Robots require a mechanism for actuating the rigid links, usually an actuator that provides the motion, torque, force, etc. However, in the case of soft robots, the actuators act as the body of the robot. Different soft actuators are described by their principle of operation, such as electroactive polymer (EAP) actuators (Bar-Cohen, 2000), shape-memory alloy (SMA) actuators (Huang, 1998), pneumatic artificial muscles (Klute, Czerniecki, & Hannaford, 1999), PneuNets Bending actuators (Polygerinos et al., 2013), reinforced actuators (Polygerinos et al., 2015).

Electroactive Polymer Actuators

Electroactive polymers (EAP) are polymers that can change their shape or size in response to the electrical stimulus (Samatham et al., 2007). EAPs are mainly classified as electronic EAPs, ionic EAPs and non-ionic EAPs based on the actuation mechanism.

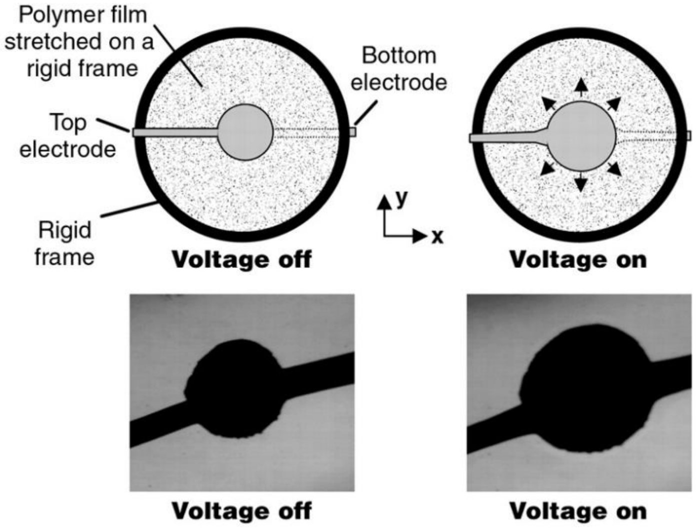

***Figure 5**: Components of dielectric elastomeric actuators and its expansion when the voltage is turned on* (Pelrine, 2000).

Dielectric Elastomer Actuator as shown in fig. 5 is a type of electronic EAP, it is made usually by coating dielectric elastomer on both sides, with a compliant electrode material (Pelrine, 2000).When an electric field is applied across the two parallel plates of a capacitor, the coulombic forces between the charges generate a stress called the Maxwell stress, causing the electrodes to move closer which makes the elastomer to expand in the lateral direction (Kofod, 2001). Ionic polymer-metal composite (IPMC) soft actuator consists of an ionic EAP layer sandwiched by two metal electrodes and when a voltage is applied to the electrodes of the actuator, it bends towards the anode direction because the hydrophilic positive ions move towards the cathode (Samaranayake, Preethichandra, Alahakoon, & Kaneto, 2007).

Shape Memory Alloy Actuators

Shape Memory Alloy (SMA) actuator has the ability to memorize and recover its original shape after it is deformed by heating over its transformation temperature (Huang, 1998). This ability of the SMA is due to shape memory effect. There are two common shape memory effects in SMA actuators they are, one-way shape memory effect, in which the deformed shape memory alloy metal returns to its original position when heated above the transition temperature and two-way memory effect, in which the material remembers two shapes at two different temperatures usually one at low temperature and one at high temperature. In two-way memory effect, the material is trained to remember both heating and cooling states (Coral, Rossi, Colorado, Lemus, & Barrientos, 2012).

Pneumatic Artificial Muscle Actuators

The first pneumatic artificial muscle was developed based on a pneumatic device that was developed in 1950’s as an orthotic appliance for polio patients by J.L.McKibben (Ching-Ping Chou & Hannaford, 1996).

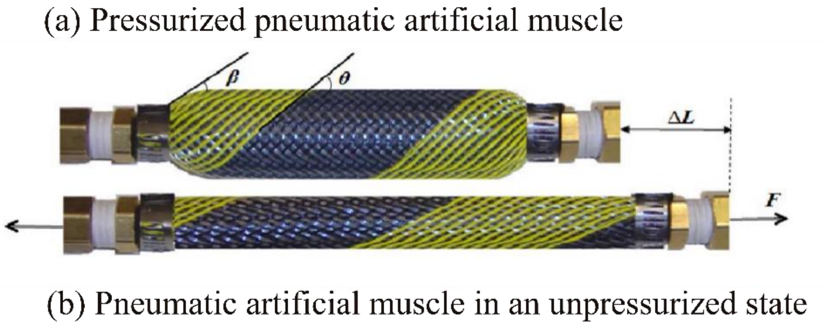

(a) Pressurized pneumatic artificial muscle

(b) Pneumatic artificial muscle in an unpressurized state

Figure 6*: Pneumatic Artifical Muscle actuator* (Doumit, Fahim, & Munro, 2009).

The McKibben muscle consists of rubber inner tube covered with a shell braided helical mesh made of flexible yet inextensible threads and clamped on both ends as shown in fig. 6. When the internal bladder is pressurized, the high-pressure gas increases the volume of the artificial muscle as it is inextensible because of the braided shell. As the volume increases, the actuator shortens and produces tension if it is coupled to a mechanical load.

PneuNets Bending Actuators

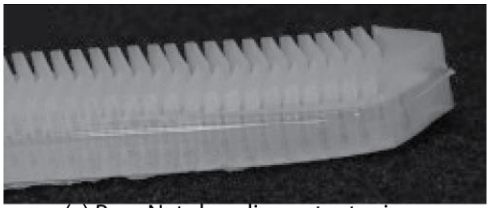

(a) PneuNets bending actuator in an unpressurized state

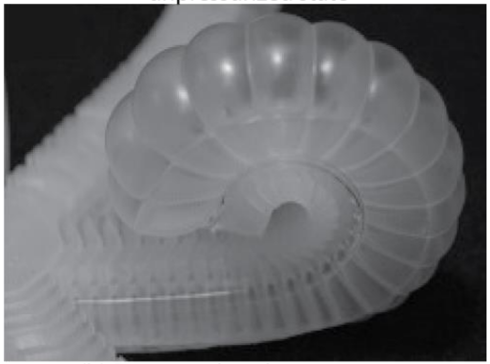

(b) PneuNets bending actuator in a pressurized state

***Figure 7**: PneuNets Bending Actuator* (Ilievski, Mazzeo, Shepherd, Chen, & Whitesides, 2011).

PneuNets Bending Actuators consists of a series of parallel chambers embedded in elastomers as repeating components as shown in fig.7(a) when pressurized the channels expand in regions that have the lowest stiffness. As the PneuNets are pressurized, in each of the single chamber the expansion in the regions having the lowest stiffness causes the chamber to bend around the axis of the channel as shown in fig. 7(b). As PneuNets bending actuator consists of a series of parallel chambers it causes an additive effect and the actuator bends and using this phenomenon the actuator can generate complex shapes (Ilievski et al., 2011).

Reinforced Actuators

Reinforced Actuators are soft actuators which are made by using a combination of an elastomeric (hyperelastic silicones) inner tube and inextensible material (fabrics and fibers) to reinforce the elastomeric chamber. Different variations in the wrapping of inextensible materials lead to various kinds of motion of the reinforced actuators.

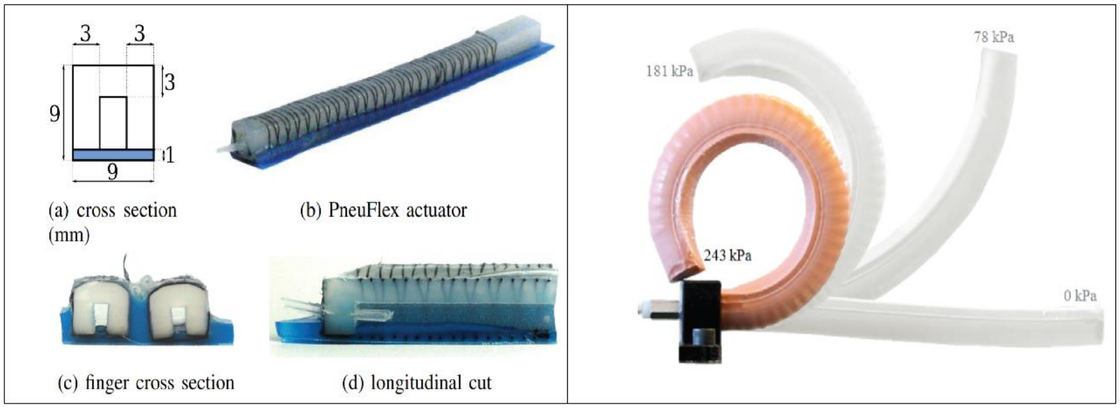

(a) PneuFlex actuator

(b) Fiber-Reinforced actuator

Figure 8*: Reinforced Actuators* (Deimel & Brock, 2013) (Galloway, Polygerinos, Walsh, & Wood, 2013).

As shown in fig. 8(a) PneuFlex actuator consists of two layers, active layer and passive layer. The active layer elongates more than the passive layer due to their physical and material properties, which causes the actuator to bend (Deimel & Brock, 2013). Fiber Reinforced Elastomeric Enclosures (FREEs) (Bishop-Moser, Krishnan, Kim, & Kota, 2012) are an example of reinforced actuators, these actuators consist of an inner latex tube which is reinforced using fibers made of cotton thread and based on the type of winding of the fiber the actuator performs different motions like axial extension, bending, twisting, rotating, etc.,. Fiber reinforced (FR)(Galloway et al., 2013) actuators consist of an inner tube with a semicircular cross-section, to which reinforcements are added on the surface as shown in fig.8(b). A fiberglass is glued to the flat surface to limit the strain which would allow the actuator to bend when pressurized.

Continuum Robotic Manipulators

Continuum robotic manipulators can be viewed as “invertebrate” robots, as compared with the “vertebrate” design of conventional rigid link robots (Walker, 2013). These robotic manipulators can perform various motions like extension, contraction, twisting, and bending. Continuum robotic manipulators are classified based on their actuation methods as follows:

a) Tendon Driven Robotic Manipulators
b) Pneumatic Robotic Manipulators
c) Hybrid Manipulators

Tendon Driven Robotic Manipulators

Cable-driven soft arm.

The Artificial Muscular Hydrostat (M. Cianchetti et al., 2011) consists of four longitudinal muscles and parallel transverse muscles whose number depends on the length of the arm. The arm elongates when the transverse muscles are squeezed, and the longitudinal muscles are relaxed. It contracts when all the longitudinal muscles contract and the transverse muscles are relaxed. The arm also bends by contraction of any one of the longitudinal muscles depending on the direction of required motion, and the contraction of the transverse muscles by a little bit in order to produce correct bending by ensuring that the diameter of the arm remains constant.

***Figure 9**: Soft Arm* (Giorelli et al., 2015).

Using these concepts of artificial muscular hydrostat, a cable-driven soft arm (Giorelli et al., 2015) has been developed by casting a silicone cone and embedding two inextensible cables with a diameter of 0.1 *mm* as shown in fig. 9. The total length of this arm is around 280 *mm*, maximum radius is 14 *mm*, minimum radius is 7 *mm*, cable distance of 2 *mm* and young modulus of 60 *kPa*.

Multi-backbone continuum arm.

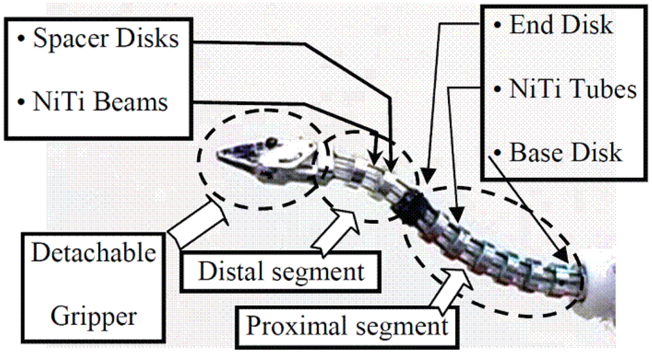

***Figure 10**: Multi-Backbone Continuum Arm* (Xu & Simaan, 2010).

The multi-backbone continuum arm is a two degree of freedom robot composed of a base disk, end disk, several spacer disks and four super-elastic NiTi tubes (Simaan, Taylor, & Flint, 2004) as shown in fig. 10. The tubes running through the disks are called the backbones of this multi-backbone continuum arm. One tube is at the center and remaining tubes are equidistant from the tube at the center. The tube at the center is attached to the base disk, end disk and to spacer disks, while all other tubes are attached only to the end disk and are free to slide or bend through holes in the base and spacer disks. Tube at the center is called primary backbone and all other tubes are called secondary backbones. The secondary backbones are used for actuating the multi-backbone continuum arm. This arm is capable of bending in any direction, which provides highly precise and accurate motions. The multi-backbone continuum arm is 4.2 mm in diameter, 28 mm in length and the NiTi tubes are 0.66 mm in diameter. Two secondary backbones are manually actuated, and the bending angle made by the arm is more than 70° sideways while applying forces larger than 1 N at the tip. The main application of this arm is minimally invasive surgeries (Simaan et al., 2009).

Pneumatically Driven Robotic Manipulators

OctArm.

The OctArm is a highly dexterous soft robotic manipulator which is designed and constructed with the inspiration from the structure, mechanics, and movements of the octopus arm (Walker et al., 2005). OctArm I consists of McKibben air muscles, which help in the movement of the arm. It has a total of 18 McKibben air muscles which help the arm to achieve different shapes and reach various positions based on the pressurization of different muscles. The 18 muscles are distributed between four segments, where first two segments have 6 actuators arrayed about the central axis and the last two segments have 3 actuators each. The actuators are arranged in this fashion so that the tapering angle of the arm is identical to the tapering angle of an octopus arm. The outer covering and the muscles connected to each other prevent the radial expansion and only allows longitudinal expansion, and by pressurizing different muscles separately, bending in the arm can be achieved. The OctArm I (figure 11(a)) manipulator has a length of 110 *cm*, weighs 18 *N* and has an inflation pressure range of 2-9 *bar*. It can lift a maximum vertical load of 12 *kg* and a transverse load of 0.5 *kg*.

(a) OctArm I

(b) OctArm V

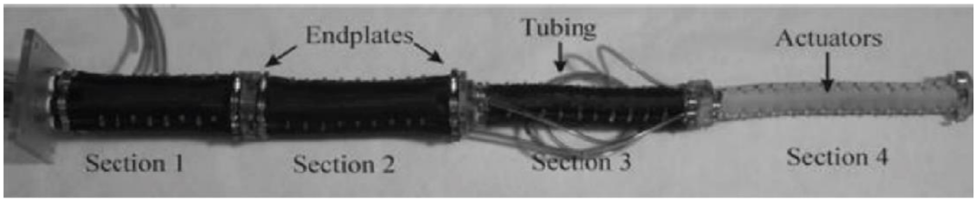

(c) OctArm IV

***Figure 11**: Different versions of OctArm* (Walker et al., 2005) (McMahan et al., 2006) (McMahan et al., 2006).

OctArm air muscle actuators have five design parameters namely, length, outer radius, tube elastic modulus, mesh angle, wall thickness. The values for these design parameters are selected based on various design requirements to provide higher extensibility with the desired elastic modulus and these parameters are tabulated in Appendix A.

OctArm IV (figure 11(c)) is divided into four sections and it has 12 degrees of freedom as each section has 3 degrees of freedom. In OctArm IV six actuators are used in sections one and two and three actuators are used in three and four. OctArm IV has a maximum pressure of 4.13 *bar*. OctArm V (figure 11(b)) is divided into three sections and it has 9 degrees of freedom as each section has 3 degrees of freedom. OctArm V has 6 actuators in section one and 3 actuators in sections two and three. OctArm V has a maximum actuation pressure of 8.27 *bar*. Two adjacent actuators in each section of these arms are considered as a channel. Various tests were performed on these OctArms by pressurizing different channels to get different values and the performance measurements are tabulated in Appendix A (McMahan et al., 2006).

Spatial fluidic elastomer manipulator.

***Figure 12**: Spatial Fluidic Elastomer Manipulator* (Marchese & Rus, 2015).

The soft spatial manipulator (figure 12) is made entirely from silicone rubbers, it comprises of serially concatenated modular segments. Each modular segment has two degrees of freedom and can move in three spatial dimensions. It is 50 *cm* long and has a mass of 0.6 *kg*. Many experiments are performed on the arm to show the compliance, durability, temperature resistance characteristics of the arm (Marchese & Rus, 2015).

Bionic Handling Assistant.

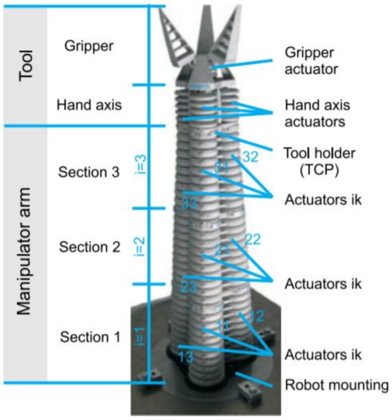

***Figure 13**: Bionic Handling Assistant* (Mahl, Hildebrandt, & Sawodny, 2014).

Bionic Handling Assistant(BHA) as shown in figure 13, is a biomimic continuum robot completely made of polyamide (Mahl et al., 2014). Each section of BHA consists of three components for spatial movement, they are base, actuator and a head region. The base and head regions are rigid plates that provide section's connectivity and actuator region is located in between these plates. Each section consists of three independently controlled pneumatic actuators arranged parallelly. These pneumatic actuators have a tapering angle of 4.5°, which gives the conical shape to the arm. The actuation of these actuators displaces the gripper by an angle of up to 30° and the arm can extend from 70 *cm* to 1.10 *m* (Grzesiak, Becker, & Verl, 2011).

Hybrid Robotic Manipulators

KSI tentacle.

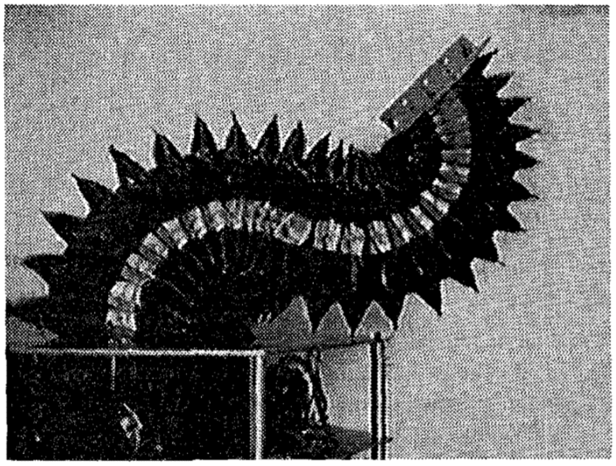

***Figure 14**: KSI tentacle* (Immega, Antonelli, & Ko, 1995).

The KSI Tentacle developed by Kinetic Sciences Inc. is a robotic manipulator based on the tentacles found in nature. The tentacle consists of a pneumatic/hydraulic bellows actuator, six tendons, a motor deck housing six tendon servo winches and optionally a gripper and a rotating wrist that can be attached at the distal end. The shape of the bladder segments has been computer-optimized to exhibit negligible shear stress in the membrane (Immega et al., 1995). Bellows of the KSI tentacle are manufactured using non-stretchable and flexible materials, which demonstrate the tentacle's overall stiffness and its extension. KSI can extend/contract using pneumatic\hydraulic bellows, contract and bend with the help of tendons.

The KSI tentacle can extend more than five times its contracted length. It can raise a load of 20 *lb.* vertically and maneuver 10 *lb.* load anywhere in its workspace. It can hold an object as small as 3.5 *inches* in diameter. The KSI tentacle can curve more than 90° in any direction and it has a payload capacity of 30 *lb.*, 20 *lb.*, 10 *lb.* at a horizontal extension of

8 *inches*, 20 *inches*, 40 *inches* respectively. Applications of KSI tentacle are nuclear decontamination of a hot cell (Immega et al., 1995), general material handling, agricultural harvesting, robotic refueling, etc.,

STIFF-FLOP manipulator.

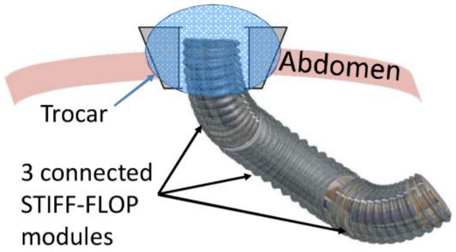

***Figure 15**: CAD model of a STIFF-FLOP manipulator* (Matteo Cianchetti et al., 2013).

The STIFF-FLOP manipulator is designed to present elongation, squeezing, bending and to show stiffness changing capability (Matteo Cianchetti et al., 2013). The STIFF-FLOP robotic manipulator has three identical modules, each module of the manipulator consists of an elastomeric cylinder with three equally spaced chambers embedded in a radial arrangement and one central hollow cavity for granular jamming, placed in a braided bellow-like structure. The bellow-like structure is created from a braided sheath which is heated after creating folds to fix them. This sheath limits the radial expansion maximizing the longitudinal expansion. For stiffness variation capability, granular jamming principle is applied by using coffee powder as granular material and latex as containing membrane. Stiffness tuning is done by changing the level of vacuum in the cavity for granular jamming.

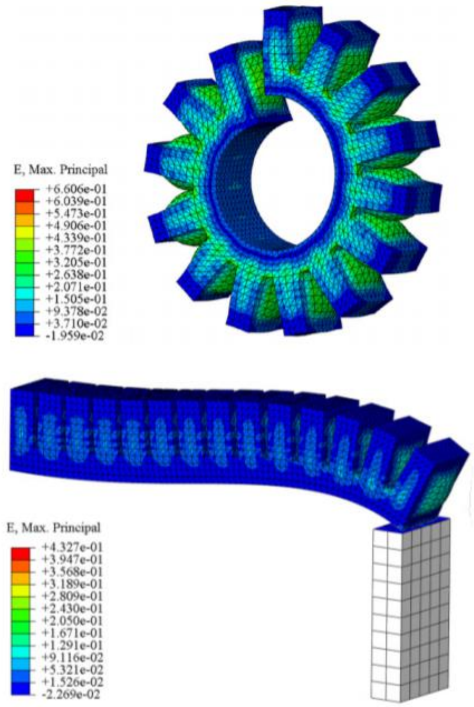

***Figure 16**: Bending response for the FEM actuator(top), Interaction of FEM actuator with a contact(bottom)* (Polygerinos et al., 2013).

Previously, different geometric parameters of pneumatic networks (PneuNets) such as the height of PneuNet, length, wall thickness, number of PneuNets are validated by running a number of simulations using a finite element method (FEM) based approach (Polygerinos et al., 2013). The performance of final actuator's design is studied using FEM. In all these FEM simulations the elastomeric components are categorized as uniform solid elements and inextensible paper layer as a shell element. Gravitational force is taken into account and pressure is acting at all the internal faces of the PneuNets. Bending ability of these actuators are assessed as shown in the fig. 16 and then experiments are conducted to demonstrate the accuracy of the computational model.

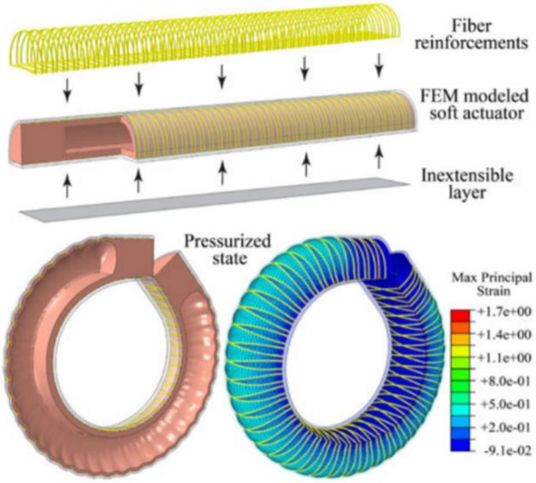

***Figure 17**: FEM modeled fiber-reinforced bending actuator(top), Bending response of a FEM actuator(bottom)* (Polygerinos et al., 2015).

Geometrical parameters and design variables that can affect the behavior of Fiber-Reinforced actuators are identified. An analytical model that captures the relationship between bending angle, input pressure and output force is developed. The response of the actuator when pressurized was studied using the insights provided by the analytical model (Polygerinos et al., 2015). A FEM model is constructed by modeling the elastomeric components of the actuator as solid tetrahedral quadratic hybrid elements and the fiber windings are modeled as quadratic beam elements. Bending response of the FEM actuator was studied by applying pressure at all the inner faces of the cavity as shown in fig. 17. To validate the analytic model and FEM models, experiments were performed.

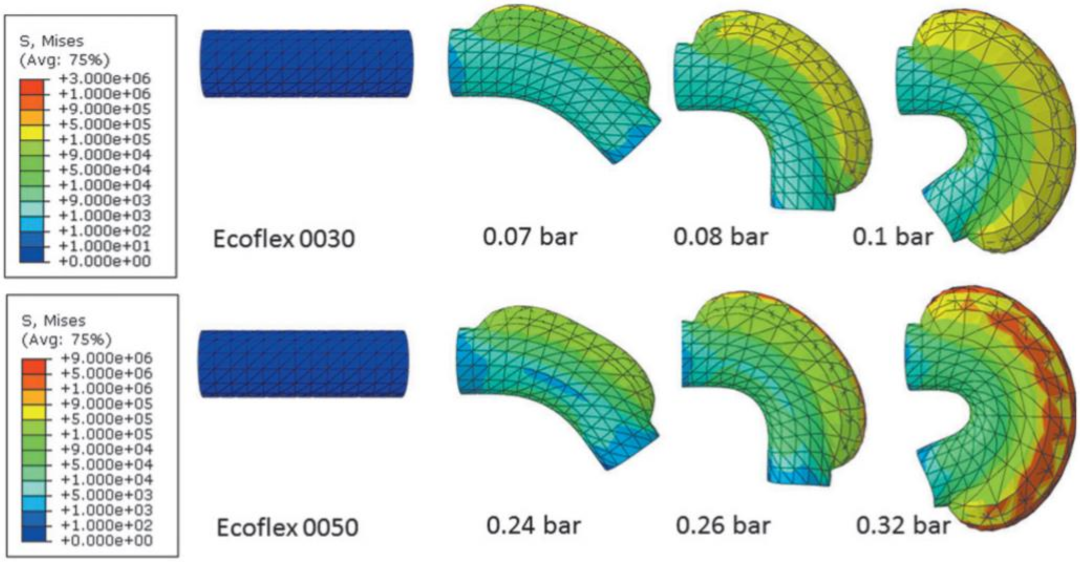

***Figure 18**: FEM simulations comparing the performance of the FEM model for two different materials* (Elsayed et al., 2014).

Computational modeling was performed to analyze the effect of the shape of the cross-section of the chambers in a pneumatic actuator module with three pneumatic chambers arranged in a triangular configuration (Elsayed et al., 2014). Comparisons were made between two different materials, by running various simulations and determining the bending angle of the tip of the module at different pressures as shown in fig. 18. The accuracy of the FEM model was evaluated against the data from an experiment of one-degree bending by actuating a single chamber.

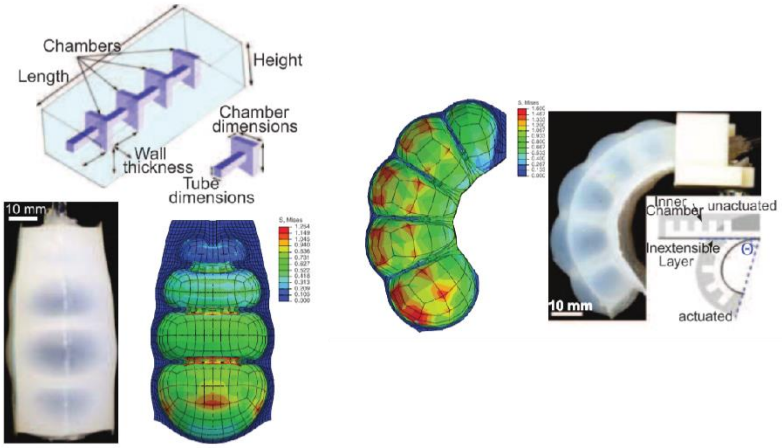

***Figure 19**: Parameters of a linear actuator, FEM and experimental results of linear and bending actuator* (Moseley et al., 2016).

An open-source simulation and design tool for soft pneumatic actuators using finite element method are made to available to the robotics research community (Moseley et al., 2016). This tool allows to create user-defined geometry and automates the process of creating geometry, meshing and applying boundary conditions. Computational modeling is performed on quarter-symmetry for linear actuator and half-symmetry for bending actuator to expedite the process and reduce the cost of computation. In this model, gravity is neglected due to the low mass of the actuators, and pressure is applied on the faces of the inner surface. The accuracy of the FEM model is investigated for both linear and bending actuator by comparing data obtained from experiments performed on linear and bending actuators. An optimization code is used to determine the optimal values of parameters based on the inputted performance characteristics of different geometric parameters.

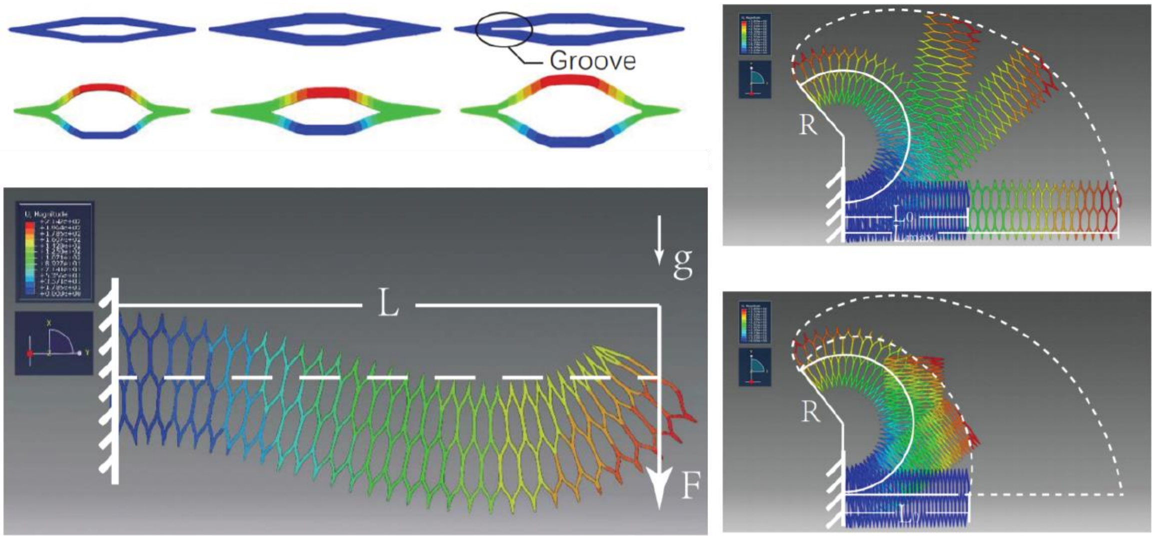

Figure 20*: Evaluation of deformation of units of HPN, load-bearing capacity, bending trajectories and boundaries of HPN* (Jiang et al., 2016).

HPN manipulator consists of a compressed honeycomb structure and pneumatic networks (Jiang et al., 2016). Various variables affecting the performance are identified and their impact is analyzed by using a computational model. Load bearing capacity of the HPN manipulator is determined by performing simulations for 42 groups of wall thickness and groove depth. Similarly, flexibility is determined by performing simulations using various combinations of the wall thickness and groove depth. Experiments were conducted to find out the deviation between the data obtained from simulations and experiment data for flexibility and load-bearing capacity.

CHAPTER 3

MATERIAL CHARACTERIZATION

In this thesis, hyperelastic silicone rubbers of shore hardness 10A (Dragon Skin 10, Smooth-On Inc., PA), 20A (Dragon Skin 20, Smooth-On Inc., PA), 30A (Dragon Skin 30, Smooth-On Inc., PA) are used to model the inner elastomeric tube of the ring-reinforced actuator and sheath of the three-chambered actuator. Computational models are used to study the effect of these materials on the axial elongation of the RRA and bending angle at the distal end tip of 3CA. Digital ABS plastic material of shore hardness 85-87D is used to model the ring reinforcements to study the effect of material properties of the ring reinforcements on the axial elongation of RRA.

The properties of these hyperelastic materials are determined by performing either tension or compression test in uniaxial, biaxial and planar directions. As the ring-reinforced actuators are not subjected compression, a tensile test of the materials is only considered. As biaxial testing requires specialized equipment, the uniaxial tensile test is considered. Uniaxial tensile testing is performed using a dumbbell-shaped test specimen, fabricated according to the ASTM D638-02a standards.


(a) Mold (b) Mold with silicone mixture (c) Test Specimen

Figure 21*: Fabrication process of a dumbbell-shaped test specimen.*

Fabrication of dumbbell-shaped test specimen is a single step process and it requires a mold (figure 21(a)) with an impression of the dumbbell-shaped test specimen with specified tolerances as per the ASTM standards (Appendix B). Two parts of silicone rubber are mixed together at a 50:50 mass ratio, degassed and poured into a mold with the cavity (figure 21(b)). Then the setup is allowed to cure at room temperature. After curing the dumbbell-shaped test specimen is removed from the mold (figure 21(c)).

The uniaxial tensile test is performed using commercially available tensile testing equipment (Instron 5944, Instron, Canton, MA). Five dumbbell-shaped test specimens of each material are tested to determine the mechanical properties. Each specimen is extended using the ASTM standards for Type IV specimens at a constant extension rate to rupture. Experimental data obtained is used to calculate stress and strain of the material. The least squares method is used to curve fit the experimental data with various hyperelastic models, such as Yeoh (Yeoh, 1993), Ogden (Ogden, 1997), or Neo-Hookean models (Ogden, 1997), to obtain material property coefficients for computational modeling.

$$U = \sum_{i=1}^{N} C_i \cdot (I_1 - 3)^i + \sum_{i=1}^{N} \frac{1}{D_i} (J_{el} - 1)^{2i} \tag{1}$$

The strain energy function shown in the equation 1 is called reduced polynomial model (Ali, 2010) for elastomeric materials, where C_i, D_i are material constants, I_1 is the first invariant of deviatoric strain, J_{el} is the elastic volume ratio and N is the number of terms in the strain energy function.

The Yeoh model for elastomeric materials is obtained by limiting the number of terms in the strain energy function to 3 and the equation for strain energy function of Yeoh model is as given in equation 2.

$$U = \sum_{i=1}^{3} C_i \cdot (I_i - 3)^i + \sum_{i=1}^{3} \frac{1}{D_i} (J_{el} - 1)^{2i} \tag{2}$$

where C_i, D_i are material constants and J_{el} is the elastic volume ratio.

The strain energy potential of Ogden model for elastomeric materials is given as shown in equation 3, it is obtained by assuming that product of the three principal stretches is 1 for incompressible materials (Ali, 2010).

$$U = \sum_{i=1}^{N} \frac{2 \cdot \mu_i}{\alpha_i^2} \cdot ({\lambda_1}^{\alpha_i} + {\lambda_2}^{\alpha_i} + {\lambda_3}^{\alpha_i} - 3) + \sum_{i=1}^{N} \frac{1}{D_i} (J_{el} - 1)^{2i} \tag{3}$$

where D_i is material constant, J_{el} is the elastic volume ratio, μ_i is the initial shear modulus, α_i is the fitting parameter , N is the number of terms in strain energy function and $\lambda_1, \lambda_2, \lambda_3$ are three principal stretches.

Neo-Hookean Model is obtained as given in equation 4, by limiting the number of terms in strain energy function to 1 and the fitting parameter α_1 is set to a value 2 in the Ogden model (Ali, 2010).

$$U = \frac{\mu_1}{2} \cdot \left({\lambda_1}^2 + {\lambda_2}^2 + {\lambda_3}^2 - 3\right) \tag{4}$$

where μ_i is the initial shear modulus and $\lambda_1, \lambda_2, \lambda_3$ are three principal stretches.

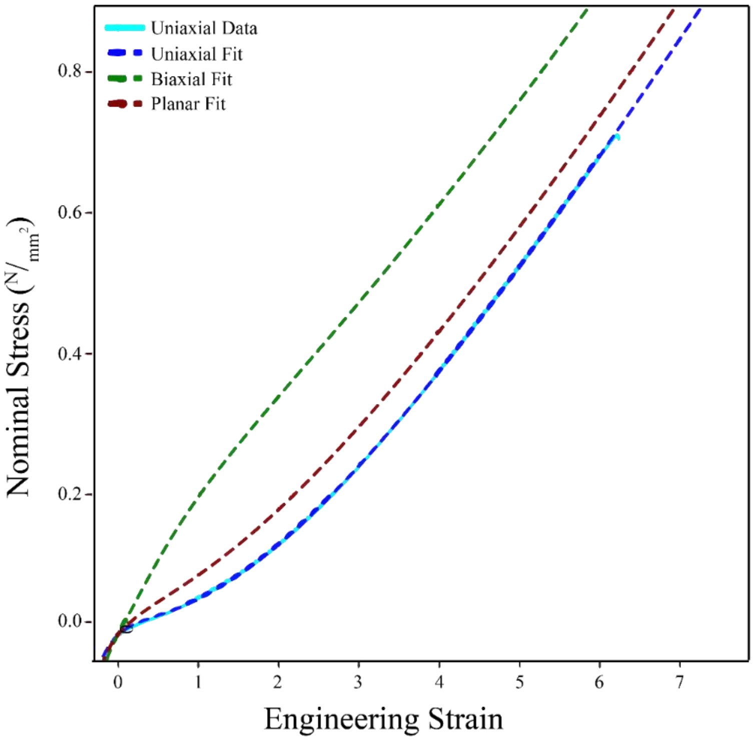

Figure 22*: Stress-Strain curves for silicone of shore hardness 10A.*

Curve fitting the experimental data obtained for the material with shore hardness 10A with the above mentioned hyperelastic models, Ogden 3rd model demonstrate the most suitable fit using an R^2 coefficient. Fig. 22 shows the stress-strain curves for the silicone with shore hardness 10A. The material coefficients obtained after testing silicone with shore hardness 10A are: $\mu 1 = 0.1802$, $\alpha 1 = -0.1997$, $\mu 2 = -0.5538$, $\alpha 2 = 1.4793$, $\mu 3 = 0.4099$, $\alpha 3 = 1.8837$, $D1 = 2.2373$, $D2 = 0$, $D3 = 0$.

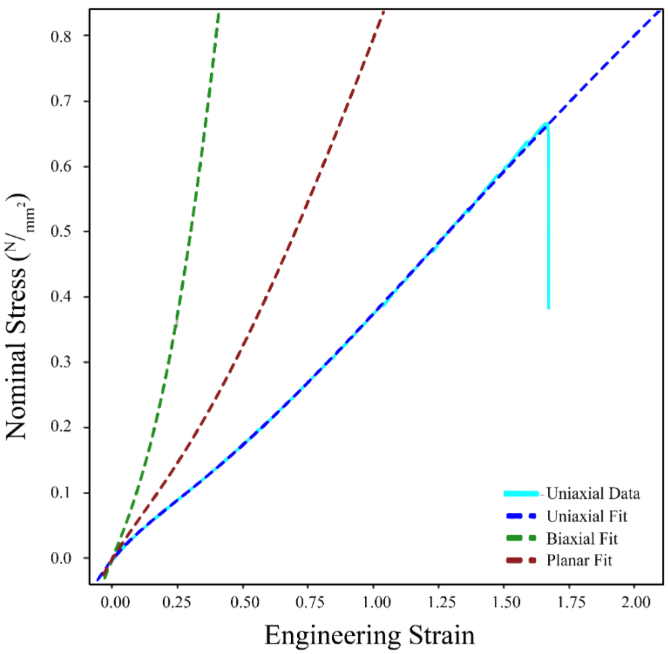

***Figure 23**: Stress-Strain curves for silicone of shore hardness 20A*

Experimental data obtained for the material with shore hardness 20A is curve fitted with hyperelastic models and Ogden 3rd model demonstrates the most suitable fit using an R^2 coefficient. Fig. 23 shows the stress-strain curves for the silicone with shore hardness 20A. The material coefficients obtained after testing silicone with shore hardenss 20A are: $\mu 1 = 1.3077, \alpha 1 = 1.1087, \mu 2 = -2.3497, \alpha 2 = -0.0317, \mu 3 = 1.2075, \alpha 3 = -1.6291, D1 = 0.4900, D2 = 0, D3 = 0.$

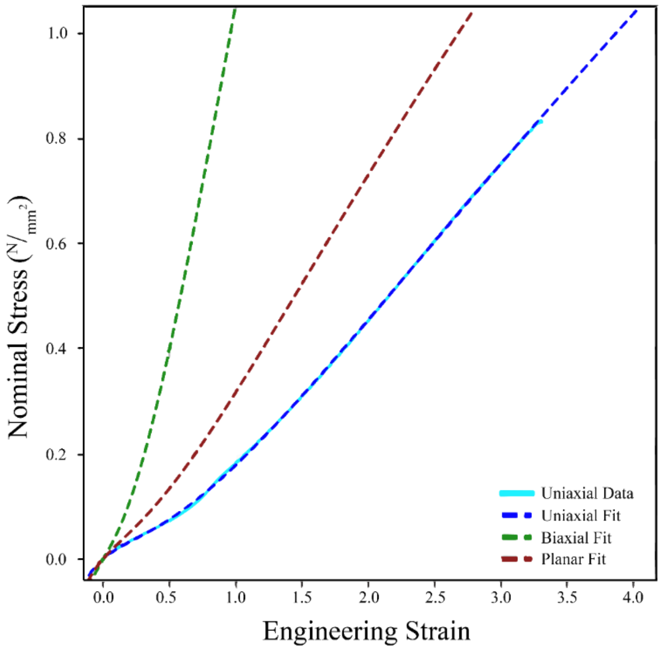

Figure 24*: Stress-Strain curves for silicone of shore hardness 30A*

Experimental Data obtained for silicone with shore hardness 30A is curve fitted with hyperelastic models and Ogden 3rd model is the best fit based on R^2 coefficient value. Fig. 24 shows the stress-strain curves for silicone with shore hardness 30A. The material coefficients obtained from curve fitting are: $\mu 1 = 1.1806$, $\alpha 1 = 1.0698$, $\mu 2 = 0.8743$, $\alpha 2 = -1.2370$, $\mu 3 = -1.9396$, $\alpha 3 = 0.1347$, $D1 = 0.7029$, $D2 = 0$, $D3 = 0$.

CHAPTER 4

DESIGN REQUIREMENTS OF THE SOFT POLY-LIMB

The Soft Robotic Arm, SPL, was developed to cater the needs of people with medical conditions such as cerebral palsy, cervical spondylotic myelopathy (CSM), etc., which affects the functioning of limb and lead to difficulties in performing activities of daily living.

Prior research studies have shown that central nervous system of humans is capable of accepting and learning to control additional limbs (Guterstam, Petkova, & Ehrsson, 2011) (Tsakiris & Carpenter, 2010). In recent studies, focus groups are assembled to understand the user's expectations and concerns regarding the usage of soft robotic limbs (Sada, Khamis, & Kato, 2017). The participants of these studies reported that soft robotic limbs should be comfortable to don and doff, be light in weight. For this reason, the maximum limit for the weight of the arm is set as 2 kg.

Anthropometry of humans shows that the length of an average male arm (Plagenhoef, Gaynor Evans, & Abdelnour, 1983) from the shoulder to the center of the wrist is 590 mm. The SPL is designed to approximately match the length of the arm. So, the desired length of SPL is 600 mm. The actuators of SPL should be pneumatically driven to reduce the number of mechanical components required.

Activities of daily living include feeding ourselves, drinking water, homemaking. To perform these activities, the minimum payload capacity at the tip of the arm is desired to be 0.5 kg. The SPL is segmented and attached together using modular connector pieces to achieve more degrees of freedom, and the desired number of segments is 3. Arms of the octopus, trunk of the elephant are tapered and similar to this, tapering is desired for SPL.

Table 1*: Design requirements of the Soft Poly-Limb.*

S. No	Requirement	Requirement Type	Desired Value
1	Weight	Physical	< 2.0 kg
2	Length	Physical	0.60 m
3	Actuation Method	Physical	Pneumatic
4	Tapering of SPL	Physical	Yes
5	Payload Capacity	Functional	> 0.5 kg
6	Wearable	Functional	Yes
7	Durability of RRA	Functional	> 1 million cycles

CHAPTER 5

RING-REINFORCED ACTUATOR

Modeling of RRA

Ring-Reinforced Actuator (RRA) consists of an inner elastomeric tube and reinforcement rings. The inner elastomeric tube when pressurized by air, the reinforcement rings restrict the radial expansion and the actuator elongates in the axial direction.

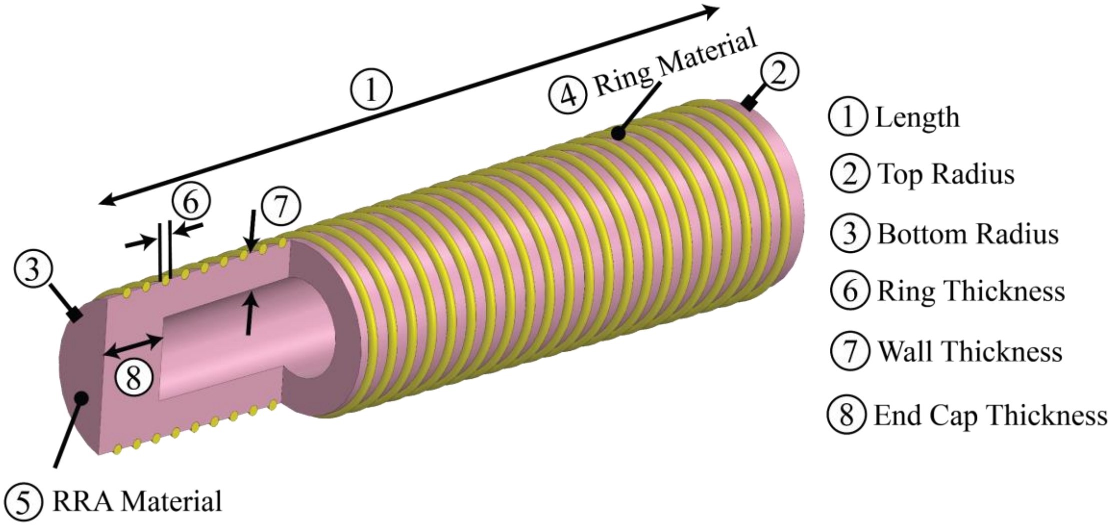

Figure 25*: Design parameters of a Ring-Reinforced Actuator.*

The list of geometric parameters and design variables involved in designing the ring-reinforced actuators are Length, Top radius, Bottom radius, Ring material, Ring count, RRA material, Ring thickness, Ring inner radius, Wall thickness, End cap thickness, as shown in fig. 25.

To analyze the effect of each design parameter on the axial elongation of RRA, FEM model is constructed, and simulations are performed with a commercially available software suite named, ABAQUS/CAE 6.14-4 (Simulia, Dassault Systemes). The inner elastomeric tube and reinforcement rings of the RRA, connected by tie constraints, are modeled using solid tetrahedral quadratic hybrid elements (ABAQUS element type C3D10H). Due to the low mass of the RRA, gravitational force is not considered in the FEM model. The dynamics of air flowing into the inner elastomeric chamber is disregarded, an inlet for the air into the tube is not taken into account and air pressure is applied to all the faces of the chamber in the RRA. Air pressure applied to the walls of the chamber is ramped up linearly in small steps of time. The criterion for determining the optimal value of the design parameters is explained below.

Length

The length of the RRA is termed Length and is denoted by $'l'$. The desired length of SPL is 600 mm and the desired number of segments is 3. So, the Length is set as 160 mm providing appreciable space for attaching segment connectors to each segment.

Bottom radius

Cross-sectional radius of the bottom of RRA is termed Bottom radius and is denoted by $'r_b'$. Bottom radius of last segment RRA is set to 9 mm due to the manufacturing limitations of fabricating ring-reinforced actuators. Bottom radius of the other segment RRAs is calculated using the formula given in equation 5.

$$(r_b)_n = (r_t)_{n+1} \tag{5}$$

where, n = number of the segment (n = 1 to 3, 1 implies first segment and 3 implies the last segment of the arm).

r_t = Top radius (section 5.1.3).

r_b = Bottom radius.

Top radius

Cross-sectional radius of the top of RRA is termed Top radius and is denoted by $'r_t'$. Top radius of RRA of each segment is calculated using equations 6 and 7.

$$(r_t)_1 = \frac{(r_b)_3}{t_r} \tag{6}$$

$$(r_t)_n = (r_b)_3 + (\frac{4-n}{3} * ((r_t)_1 - (r_b)_3) \tag{7}$$

where, t_r = Ratio of the Bottom radius of the last segment RRA to the Top radius of the first segment RRA (section 6.1.2),

n = number of the segment (n = 1 to 3, 1 implies first segment and 3 implies last segment of the arm),

r_t = Top radius,

r_b = Bottom radius.

Ring material

Existing Kevlar reinforced actuators are prone to large stress concentrations at the reinforcement contact points on the elastomeric inner tube leading to the reduced operational lifecycle. To increase the operational lifecycle, investigations on the performance of the reinforced actuators with helical, double helical reinforcements made out of stiffer polyurethane rubber (PMC 790, Smooth-On Inc.,) were conducted, but due to laborious and arduous manufacturing process involved in making these reinforcements, ring-based reinforcements made of digital ABS plastic material (Young's modulus, E = 2,620 MPa; Poisson's ratio, v = 0.35) are chosen instead of helical reinforcements. Digital ABS ring reinforcements reduce the problems involved in fabricating reinforcements and increase the contact surface area between the reinforcements and the surface of the inner elastomeric tube.

Ring count

Number of reinforcing rings on RRA is termed Ring count and denoted by $'n_r'$. To investigate the Ring count required to maximize axial elongation, the material properties of the inner elastomeric tube in the FEM model are varied with properties of silicone of shore hardness 10A, 20A and 30A. Material properties of digital ABS plastic are used for reinforcement rings in the FEM model. All other design parameters are set with arbitrary values as shown in table 2.

***Table 2**: Number of nodes and elements of FEM models used to study the effect of ring count.*

Length (mm)	Normalized Ring Count	RRA Material	Number of Nodes	Element Type	Number of Elements
160	0.125	Shore 10A Silicone	175566	C3D10H	113528
160	0.250	Shore 10A Silicone	203219	C3D10H	126919
160	0.375	Shore 10A Silicone	231021	C3D10H	140423
160	0.500	Shore 10A Silicone	259067	C3D10H	154135
160	0.625	Shore 10A Silicone	286595	C3D10H	167375
160	0.125	Shore 20A Silicone	175566	C3D10H	113528
160	0.250	Shore 20A Silicone	203219	C3D10H	126919
160	0.375	Shore 20A Silicone	231021	C3D10H	140423
160	0.500	Shore 20A Silicone	259067	C3D10H	154135
160	0.625	Shore 20A Silicone	286595	C3D10H	167375
160	0.125	Shore 30A Silicone	175566	C3D10H	113528
160	0.250	Shore 30A Silicone	203219	C3D10H	126919
160	0.375	Shore 30A Silicone	231021	C3D10H	140423
160	0.500	Shore 30A Silicone	259067	C3D10H	154135
160	0.625	Shore 30A Silicone	286595	C3D10H	167375

Number of reinforcement rings on the RRA in the FEM model is varied using the equation 8.

$$n_r = \frac{l}{d_r} \times r \qquad (8)$$

where, l = length of the actuator,

d_r = diameter of the ring,

r = normalized ring count.

For example, if the length of the actuator = 160 mm, diameter of the ring is 2 mm and normalized ring count is 0.25 then the number of rings calculated using equation 8 is 20. Normalized ring count is the ratio of number of rings with set diameter to the maximum number of rings with set diameter possible without intersection. Simulations are performed using FEM model with Ring count calculated using normalized ring count of 0.125, 0.250, 0.375, 0.500, 0.625. The scale for the magnitude of the displacement for every model and the FEM simulation results are shown in figure 27 and 28, for silicone with shore hardness 10A, 20A and 30A.

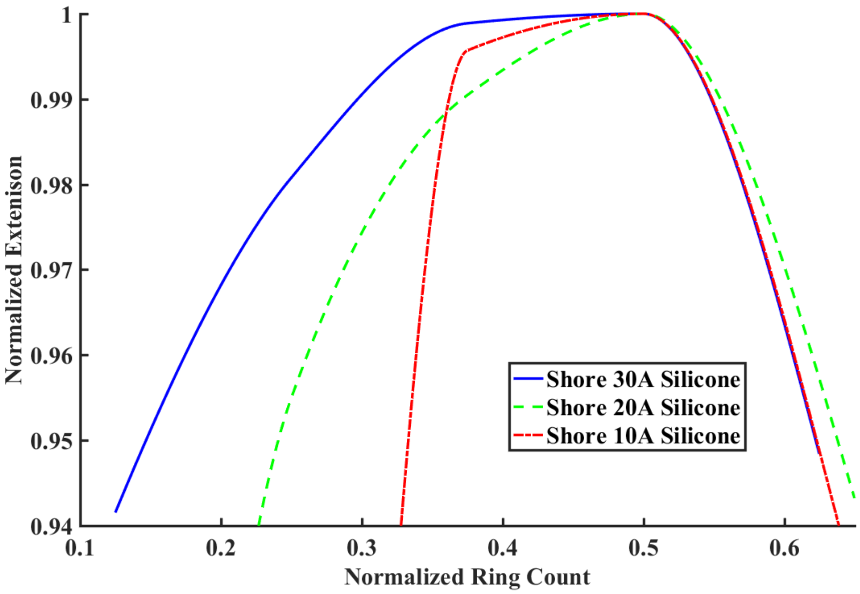

***Figure 26**: Normalized extension vs. normalized ring count plot for RRA with silicone of shore hardness 30A, 20A and 10A.*

(a) Shore 10A Silicone RRA with normalized ring count 0.125

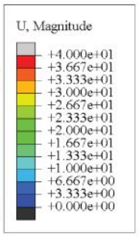

(b) Shore 10A Silicone RRA with normalized ring count 0.250

(c) Shore 10A Silicone RRA with normalized ring count 0.375

(d) Shore 10A Silicone RRA with normalized ring count 0.500

(e) Shore 10A Silicone RRA with normalized ring count 0.625

***Figure 27**: Displacement contours of shore 10A silicone RRA FEM model for different normalized ring counts.*

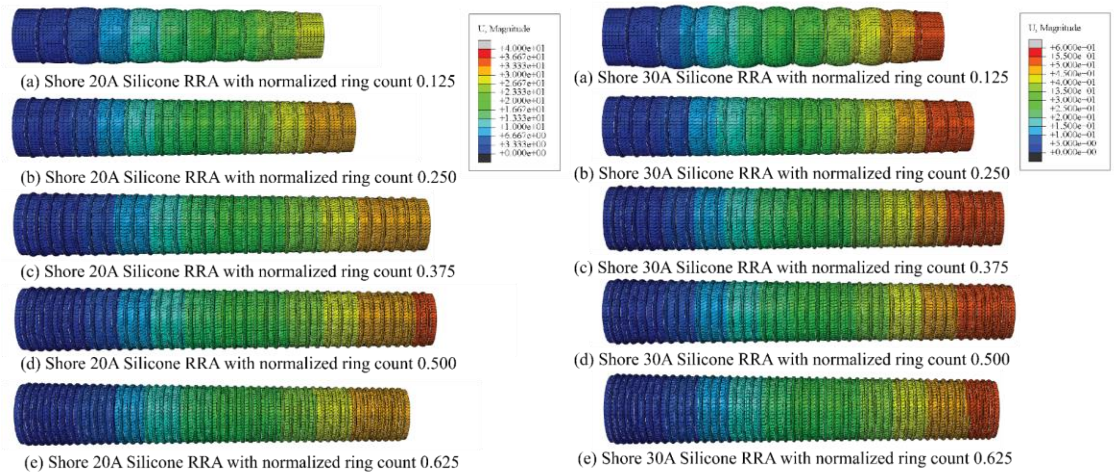

(a) Shore 20A Silicone RRA with normalized ring count 0.125

(b) Shore 20A Silicone RRA with normalized ring count 0.250

(c) Shore 20A Silicone RRA with normalized ring count 0.375

(d) Shore 20A Silicone RRA with normalized ring count 0.500

(e) Shore 20A Silicone RRA with normalized ring count 0.625

(a) Shore 30A Silicone RRA with normalized ring count 0.125

(b) Shore 30A Silicone RRA with normalized ring count 0.250

(c) Shore 30A Silicone RRA with normalized ring count 0.375

(d) Shore 30A Silicone RRA with normalized ring count 0.500

(e) Shore 30A Silicone RRA with normalized ring count 0.625

Figure 28*: Displacement contours of shore 20A silicone and shore 30A silicone RRA FEM models for different normalized ring counts.*

The axial elongation of the RRA for each simulation is calculated from the results obtained by simulating FEM models (figure 28) of the actuator reinforced with different normalized ring counts. These calculated values of axial elongation are normalized and plotted against normalized ring count as shown in figure 26. From data, it can be observed that there is a gradual increase in axial elongation from normalized ring count 0.125 to 0.500 and decrease in elongation from normalized ring count 0.5 to 0.625, but the increase in elongation from normalized ring count 0.375 to 0.5 is 0.43 % for shore 10A silicone, 0.95 % for shore 20A silicone, 0.1 % for shore 30A silicone. Therefore, the normalized ring count 0.375 is chosen to calculate the number of reinforcement rings required as it reduces the number of rings on each actuator and the overall weight of the arm compared to the normalized ring count 0.5.

RRA Material

The material of the inner elastomeric tube termed RRA Material is varied in the FEM model to study its effect on the axial elongation of the RRA. Values of parameters such as

Length, Ring count, Ring material in the FEM model are set as discussed in previous sections (table 3) and all other parameters are set arbitrarily.

Table 3*: Number of nodes and elements of FEM models used to study the effect of RRA material.*

Length (mm)	Normalized Ring Count	RRA Material	Ring Material	Number of Nodes	Element Type	Number of Elements
160	0.375	Shore 10A Silicone	ABS	231021	C3D10H	140423
160	0.375	Shore 20A Silicone	ABS	231021	C3D10H	140423
160	0.375	Shore 30A Silicone	ABS	231021	C3D10H	140423

The results obtained from simulations of these FEM models are used to calculate the axial elongation of RRA and normalized extension values are plotted against normalized pressure as shown in figure 29. The graph shows that FEM model with shore 10A silicone material has a higher axial extension at a normalized pressure of 0.25 when compared to the plots of other silicone FEM models. FEM model with shore 10A silicone RRA has higher normalized extension followed by shore 30A silicone and shore 20A silicone as shown in figure 30. The extension of RRA FEM model with shore 30A silicone is higher than the FEM model with shore 20A silicone as the tensile strength of shore 20A silicone is higher.

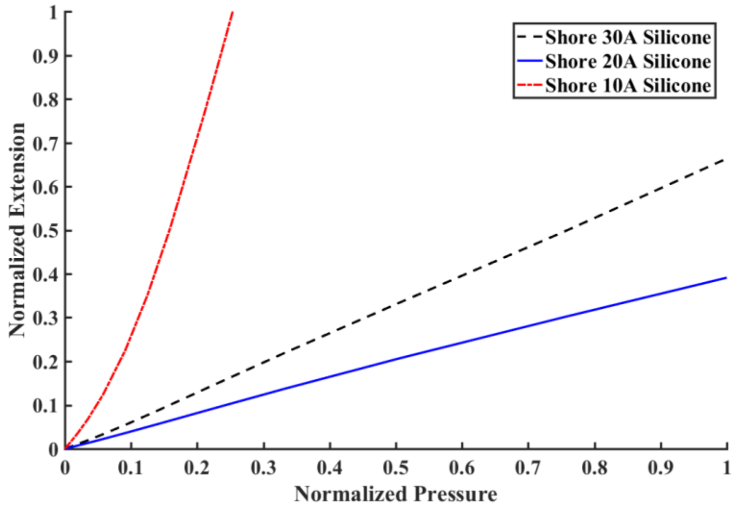

***Figure 29**: Normalized extension vs. normalized pressure plot for RRA with silicone of shore hardness 30A, 20A and 10A.*

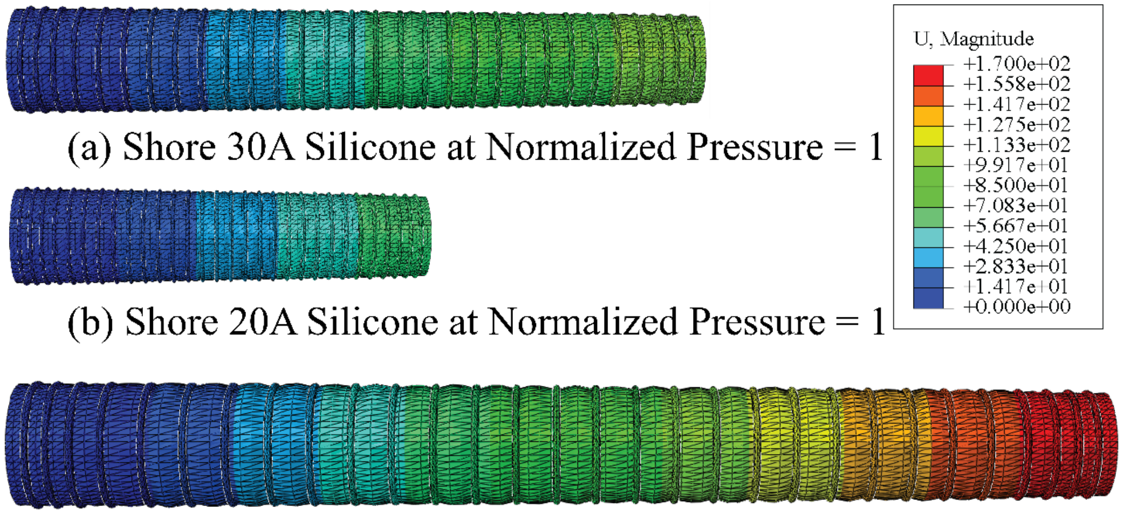

(a) Shore 30A Silicone at Normalized Pressure = 1

(b) Shore 20A Silicone at Normalized Pressure = 1

(c) Shore 10A Silicone at Normalized Pressure = 0.25

***Figure 30**: Displacement contours of RRA with silicone of shore hardness 10A, 20A and 30A FEM model for different normalized pressures.*

The tensile strength of materials investigated for the inner elastomeric tube 475 psi, 550 psi, 500 psi, for shore 10A silicone, shore 20A silicone, and shore 30A silicone respectively. The results from simulations show that materials with lowest tensile strength have highest axial elongation. To increase the robustness of the RRA, shore 30A silicone is chosen as the material for the inner elastomeric tube as it delivers the best compromise between tensile strength, axial elongation and actuation pressure.

Ring Thickness

The thickness of the ring is termed Ring Thickness and is denoted by $'d_r'$. The Ring Thickness is varied in the FEM model for studying its effect on the axial elongation of RRA. In the FEM model, digital ABS plastic material's properties are assigned to ring reinforcements and shore 30A silicone material's properties are assigned to the inner elastomeric tube. Normalized ring count is set as 0.375 and arbitrary values are set for all other design parameters as shown in table 4.

***Table 4**: Number of nodes and elements of FEM models used to study the effect of thickness of the ring.*

Length (mm)	Normalized Ring Count	RRA Material	Ring Material	Number of Nodes	Element Type	Number of Elements
160	0.375	Silicone with shore hardness 30A	ABS	231021	C3D10H	140423
160	0.375	Silicone with shore hardness 30A	ABS	234357	C3D10H	142193
160	0.375	Silicone with shore hardness 30A	ABS	252678	C3D10H	155424

Simulations are performed, and the data obtained is used to plot normalized extension against normalized ring thickness as shown in fig. 31. X-axis describes the normalized ring thickness, where 1 describes the maximum thickness of the rings that can be placed on the RRA without intersection. Y-axis describes the normalized extension, where 1 on the y-axis describes the maximum extension achieved. The normalized thickness range of 0.1 to 0.4 is eliminated from the study due to the difficulties in manufacturing rings with smaller thickness.

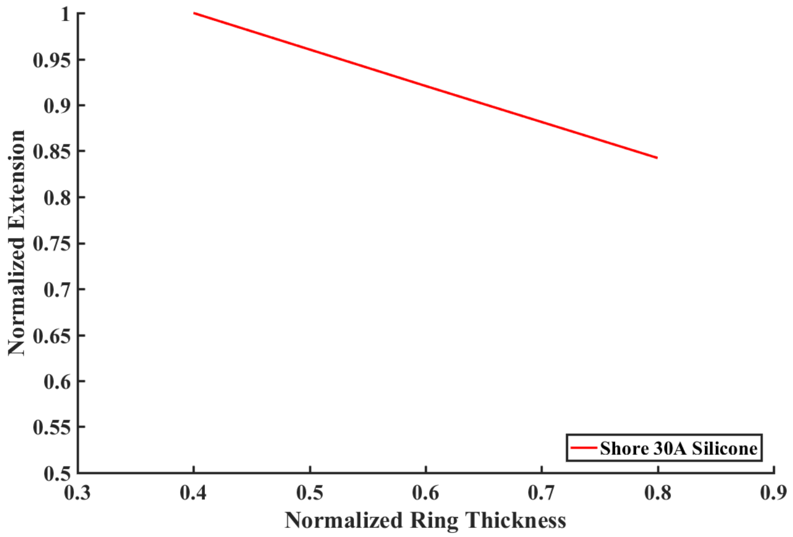

Figure 31*: Normalized extension vs. normalized ring thickness plot for RRA with silicone of shore hardness 30A.*

(a) Normalized Ring Thickness of 0.4

(b) Normalized Ring Thickness of 0.6

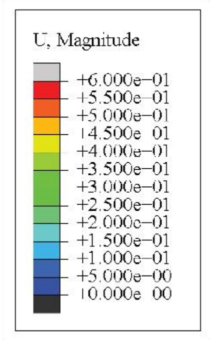

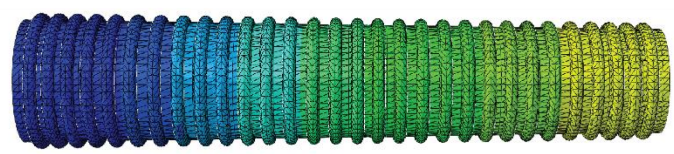

(c) Normalized Ring Thickness of 0.8

Figure 32*: Displacement contours of RRA with silicone of shore hardness 30A FEM model for different normalized ring thicknesses.*

The results from the simulations of finite element model (figure 32) show that as the normalized ring thickness increases, the axial elongation of drops. So, the normalized ring thickness of 0.4 is chosen as the best value for to calculate the design variable Ring Thickness.

Inner radius of the ring

The inner radius of the rings becomes incrementally smaller as they are designed to fit the tapering size of the actuator. The inner radius of the ring varies as per the formula in the equation below:

$$x_{(r_n)} = 2 \cdot r_b + \frac{2 \cdot (r_t - r_b) \cdot r_n}{n_r} \tag{9}$$

where, $x_{(r_n)}$ = Inner radius of the ${r_n}^{th}$ ring,

n_r = number of rings,

r_n = ring number (1 to 30 from the bottom of RRA to the top of RRA).

Wall thickness of RRA

The thickness of the walls of RRA is termed Wall thickness of RRA. It is varied in the FEM model to study its effect on the axial elongation of RRA. All other design variables and geometric parameters are set in the FEM models as shown in table 5.

Table 5*: Number of nodes and elements of FEM models used to study the effect of Wall thickness of RRA.*

Length (mm)	Normalized Ring Count	Normalized Wall Thickness	RRA Material	Number of Nodes	Element Type	Number of Elements
160	0.375	0.2	Shore 30A Silicone	191948	C3D10H	109673
160	0.375	0.333	Shore 30A Silicone	206941	C3D10H	121627
160	0.375	0.466	Shore 30A Silicone	231021	C3D10H	140423
160	0.375	0.6	Shore 30A Silicone	240858	C3D10H	148557
160	0.375	0.733	Shore 30A Silicone	245289	C3D10H	152649

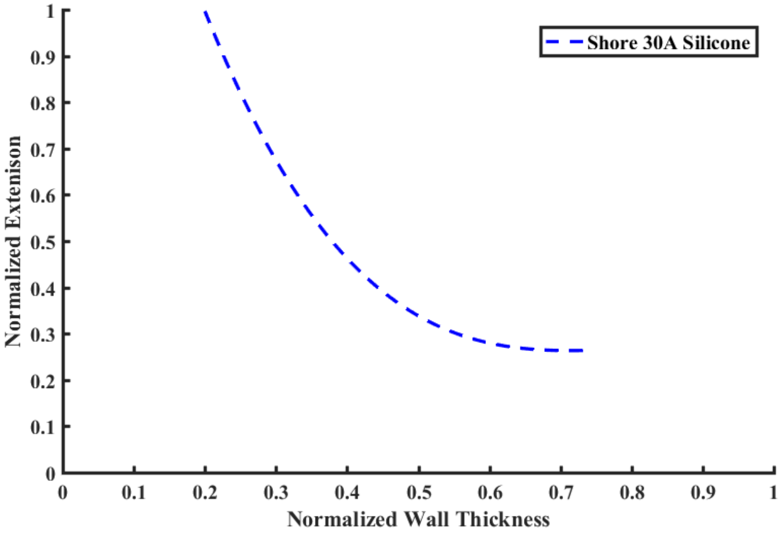

Figure 33*: Normalized extension vs. normalized wall thickness plot for RRA with silicone of shore hardness 30A.*


(a) Normalized Wall Thickness of 0.200


(b) Normalized Wall Thickness of 0.333


(c) Normalized Wall Thickness of 0.466

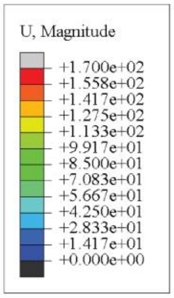


(d) Normalized Wall Thickness of 0.600


(e) Normalized Wall Thickness of 0.733

Figure 34*: Displacement contours of RRA with silicone of shore hardness 30A FEM model for different normalized wall thicknesses.*

In fig.33, normalized wall thickness is plotted on the x-axis and normalized extension is plotted on the y-axis and the curve is a decreasing exponential curve. From the graph, the axial elongation of RRA decreases as the Wall thickness of RRA increases at the same actuation pressure. So, to achieve the best compromise between maximum actuation pressure and maximum elongation of the actuator a normalized wall thickness of 0.466 is chosen.

End cap thickness of RRA

The thickness of the caps at both ends is termed as End cap thickness of RRA and it is varied to study the effect of thickness of the cap on the axial elongation of the RRA. In the FEM model, digital ABS material's properties are assigned to the ring reinforcements, shore 30A silicone material's properties are assigned to the inner elastomeric tube, normalized ring count of 0.375 is used to calculate the Ring count, normalized wall thickness is chosen to be 0.47 and all other design variables are set arbitrarily. The results from the computational models are plotted as a graph as shown in figure 36.

Table 6*: Number of nodes and elements of FEM models used to study the effect of End cap thicknesses of RRA.*

Length (mm)	Normalized End Cap Thickness	RRA Material	Number of Nodes	Element Type	Number of Elements
160	0.125	Shore 30A Silicone	225280	C3D10H	135593
160	0.25	Shore 30A Silicone	231021	C3D10H	140423
160	0.5	Shore 30A Silicone	222503	C3D10H	135219
160	0.75	Shore 30A Silicone	223824	C3D10H	137123

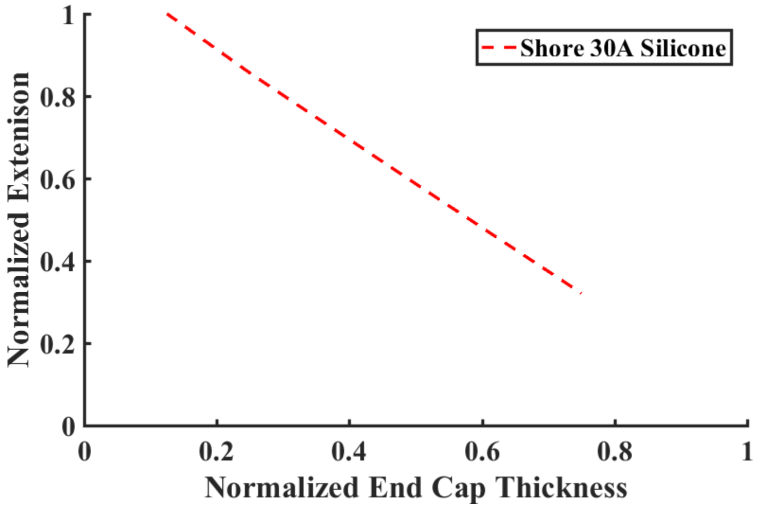

Figure 35*: Normalized extension vs. normalized end cap thickness plot for RRA with silicone of shore hardness 30A.*

(a) Normalized End Cap Thickness of 0.125

(b) Normalized End Cap Thickness of 0.250

(c) Normalized End Cap Thickness of 0.500

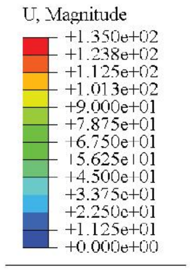

(d) Normalized End Cap Thickness of 0.750

Figure 36*: Displacement contours of RRA with silicone of shore hardness 30A FEM models for different normalized end cap thicknesses.*

The graph (figure 35) shows a linear decrease in the axial extension as the end cap thickness of RRA increases. So, the normalized end cap thickness of 0.25 is chosen as the RRA with normalized end cap thickness less than 0.25 has a ballooning effect at the ends and higher end cap thickness reduces the extension of the actuator.

Summary of modeling of RRA

After performing various simulations to study the effect of each individual parameter on the behavior of RRA, optimal values for the parameters are selected as per the design requirements and are tabled in table 7. Length of the actuator is set to 160 mm to make the SPL approximately to the length of a human arm. Silicone Material of shore hardness 30 A is set as the material for the inner elastomeric tube of the RRA to achieve higher axial elongation and to retain the robustness of the RRA. Digital ABS plastic is used to fabricate the rings to reduce the difficulties in the manufacturing of rings and to achieve higher elongation with lower stress concentration at the contact surface. Normalized ring count of 0.375 is used to calculate the number of rings as it provides comparably higher elongation with lesser number of rings leading to lesser weight of the RRA. Normalized ring thickness of 0.400 is chosen as it provides the maximum axial elongation. Normalized wall thickness of 0.466 is chosen to increase the robustness of the RRA by withholding higher actuation pressure. Normalized end cap thickness of 0.250 is chosen to reduce the ballooning effect at the end of the RRA and to achieve higher axial elongation.

Table 7*: Optimal values for various design parameters.*

S. No	Parameter	Optimal Value/Material
1	Length	160 mm
2	RRA Material	Shore 30A Silicone
3	Normalized Ring Count	0.375
4	Ring Material	Digital ABS plastic
5	Normalized Ring Thickness	0.400
6	Normalized Wall Thickness	0.466
7	Normalized End Cap Thickness	0.250

Fabrication of RRA

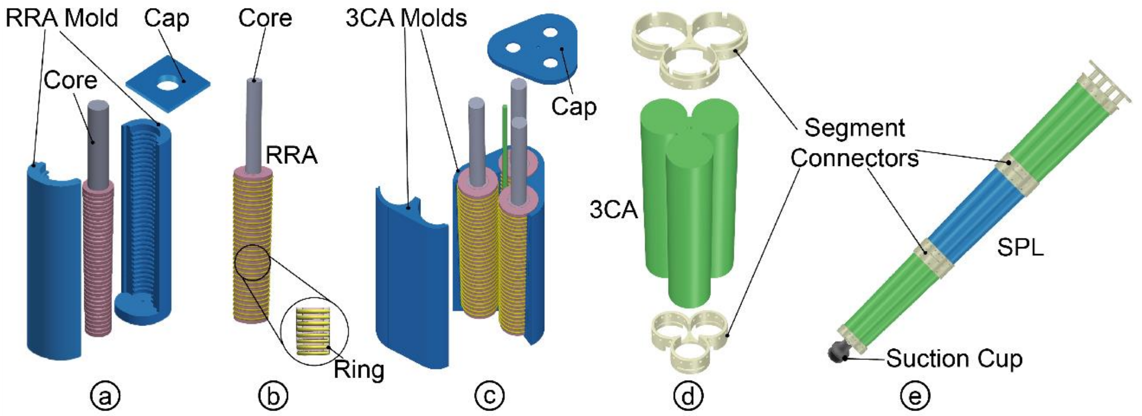

Mold Setup for fabricating inner elastomeric tube of RRA

Uncapped RRA

Mold Setup for bonding RRAs into 3CA with outer elastomeric sheath

3CA with segmnet connectors

Soft Poly-Limb

Figure 37*: Fabrication process of SPL and its components.*

To fabricate the Ring-Reinforced actuators, molds are modeled using a CAD software (SolidWorks, Dassault Systemes, FRA) and fabricated using high spatial resolution 3D printers (Objet350, Stratasys, MN and Fortus450, Stratasys, MN). The mold for fabricating the inner elastomeric tube consists of four parts: a two-part shell, a frustum-shaped core, and a cap, as shown in figure 37(a). The two-part shell is designed with extruded features to create evenly spaced, incrementally smaller, semi-circular impressions on the inner elastomeric tube of RRA for placement of the reinforcement rings. The frustum-shaped core is designed to create a uniformly tapered chamber in the inner elastomeric tube and a dowel pin is attached to the center of the bottom of the core to achieve the desired concentricity within the mold. The top cap is designed to hold the two-part shell and the core in place to create a uniform RRA during the curing process.

Two parts namely Part A and Part B of the silicone of shore hardness 30 A are mixed as per the ratio mentioned by the manufacturers, degassed to remove any air bubbles and then poured into the cavity of the two-part shell, which are secured together firmly. Then the frustum-shaped core is placed to create a cavity and the top cap is used to close the mold and align the core to the center of the mold. The final setup is placed in an oven at 60 °C to expedite the silicone mixture curing process.

The reinforcement rings are modeled using a CAD modeling software and 3D printed with a digital ABS material (RGD531, Stratasys, MN) using an objet350 3D printer (Stratasys, MN). The rings are made to fit the tapering of the inner elastomeric tube, thus becoming incrementally smaller at each passing rung.

The 3D printed reinforcement rings are made to sit in the semi-circular impressions on the cured inner elastomeric tube as shown in figure 37(b), then the core is removed from the actuator and ends are capped to required thickness to complete the fabrication of the RRA.

Evaluation of RRA

Linear Expansion Test

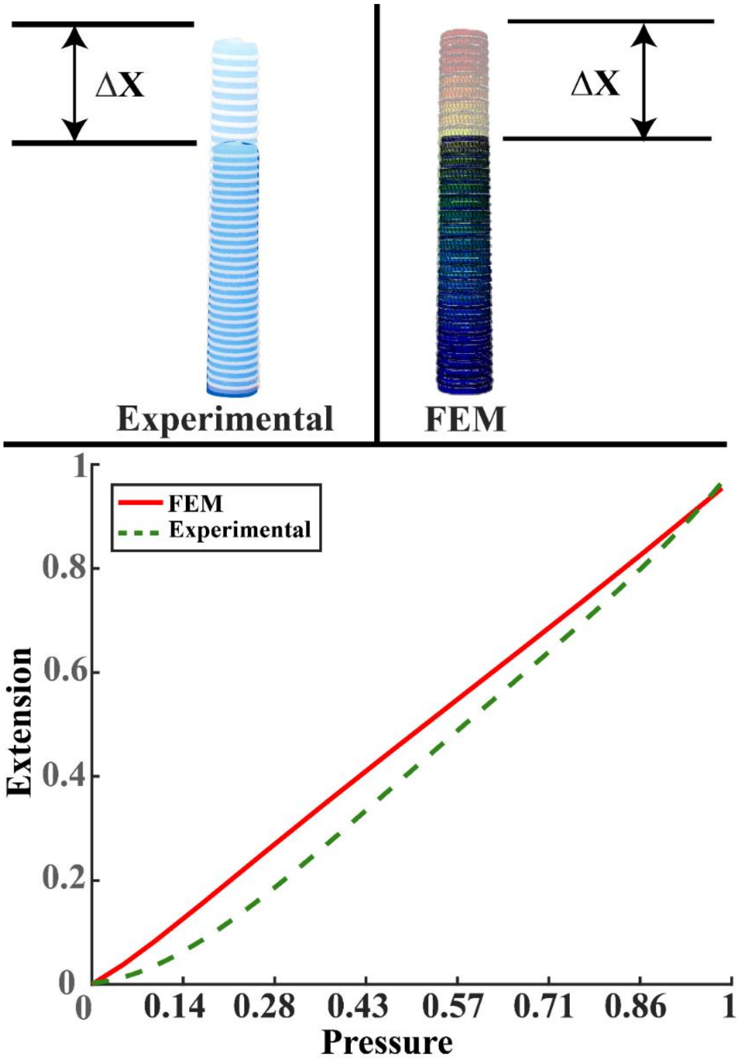

***Figure 38**: Extension vs Pressure plot from FEM and experimental data of RRA.*

To compare the results obtained from the simulations of quasi-static computational models with the experimental data of the RRA, a linear extension test is performed. To perform the linear extension test, an RRA is fabricated as explained in the previous section and a small plastic attachment is 3D printed to limit the extension of the RRA to one direction.

The small plastic attachment is attached to the bottom of the RRA and it is mounted on a fixture to hold the RRA with the top facing upwards and the bottom part fixed. Passive reflective markers are attached to the top and base of the RRA to obtain position data of the RRA in real time with the aid of motion capture cameras. The actuator is pneumatically pressurized in small increments up to a pressure of 206.8 kPa and data is collected for five trails. Data obtained from the experiment is averaged and compared to the data obtained from the simulations of FEM and data demonstrates a maximum displacement error of 0.54% at the bottom end of the actuator when fully extended, an RMS error of 5.1 mm on the entire extension data.

Fatigue Test

To compare the operational life of Fiber-Reinforced actuators and the Ring-Reinforced actuators, both the actuators are cyclically pressurized from 0 to 206.8 kPa in an identical test setup. Two actuators having identical geometrical parameters, identical material properties for the inner elastomeric tube are cyclically pressurized and depressurized until a dramatic increase or drop in the pressure, which indicates the failure of the actuators. The results obtained from the experiment indicate that the Fiber-Reinforced actuators have an average operational lifecycle of 130,000 cycles and the Ring-Reinforced actuators have an average operational lifecycle of 1,100,000 cycles. These results indicate that RRAs have a higher operational life than Fiber-Reinforced actuators. One of the reasons for this reduced operational lifecycle of Fiber-Reinforced actuators is, the ring reinforcements in RRA's have larger contact surface area compared to the Fiber-Reinforced actuators which reduce the stress concentrations at the intersections of the inner elastomeric tube and the reinforcements.

CHAPTER 6

THREE-CHAMBERED ACTUATOR

Modeling of 3CA

The three-chambered actuator consists of three RRA’s, an outer elastomeric sheath and an elastomeric core. The three RRA’s are arranged in an equilateral triangular fashion with uniform spacing between RRA’s and are enclosed by the elastomeric sheath, bonded by the elastomeric core as shown in the fig. 39. 3CA has three degrees of freedom, one translational and two rotational, which allows for better maneuverability of the soft robotic arm. Pressurizing three actuators simultaneously leads to translational motion and pressurizing any one actuator or two actuators simultaneously bends the 3CA towards the remaining actuators as other actuators act as strain limiting agent limiting the elongation of the actuator.

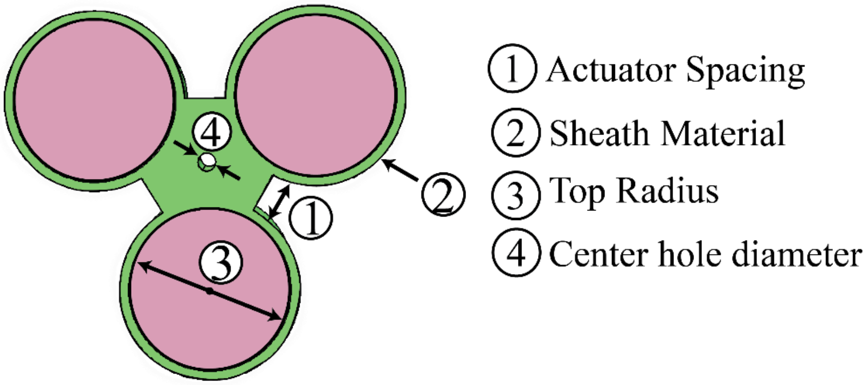

Figure 39*: Design parameters of 3CA.*

The design variables and geometrical parameters involved in designing the three-chambered actuators are Actuator Spacing, Taper Ratio, Sheath Material, Thickness of the Sheath and Center Hole Diameter are shown in figure 39.

A quasi-static FEM model of 3CA is constructed to analyze the effect of various design parameters on the bending angle of 3CA using a software suite named, ABAQUS/CAE 6.14-4 (Simulia, Dassault Systemes). Bending angle is the angle made by the bottom face of the 3CA with the top face of the 3CA. Normalized bending angle is the ratio of bending angle of the actuator at certain air pressure over the maximum bending angle required (90º in the case of SPL). The inner elastomeric tube and reinforcement rings of each RRA are constrained with tie constraints, the sheath of the 3CA and RRAs are constrained using another set of tie constraints. An ENCASTRE boundary condition is applied to the top face of the 3CA, i.e., the top face of the RRA's and the top face of the sheath. 3CA is meshed using solid tetrahedral quadratic hybrid (C3D10H) elements. Pressure is applied to all the faces of the chamber of two RRAs to bend the 3CA model and ramped up linearly in small steps of time. Gravitational force is applied on to the whole model in the opposite direction of bending. The dynamics of airflow and inlet for the air are not taken into account in these FEM models. The thickness of the sheath is set to 2 mm, as the main purpose of the outer sheath is to hold the RRAs in place and as prior investigations show that having higher thickness effects the bending angle 3CA. The values for the design parameters are determined based on the results from various simulation results of these finite element models and criteria for selection of the values for the variables is explained in the following sections.

Actuator Spacing

In a three-chambered actuator, three RRA's are bonded together by an elastomeric sheath and an elastomeric core. There is a uniform spacing between each actuator, this spacing is termed Actuator Spacing and is denoted by $'s'$. To study the effect of spacing between the actuators on the bending angle of the three-chambered actuator, computational modeling is performed using the FEM model discussed above. Initially, Shore 30A silicone material's properties are set to the sheath, a taper ratio (section 6.1.2) of 0.5 is used, optimal values for design parameters of RRA are used as discussed in the previous chapter, and all other parameters are set arbitrarily in these FEM models (table 8). The spacing of actuators is varied from $3 \cdot s\ mm$ to $9 \cdot s\ mm$, where an arbitrary value is chosen for 's'.

***Table 8**: Number of nodes and elements of FEM models used to study the effect of actuator spacing.*

Actuator Spacing (mm)	Sheath Material	Number of Nodes	Element Type	Number of Elements
$3 \cdot s$	Shore 30A Silicone	348390	C3D10H	197156
$6 \cdot s$	Shore 30A Silicone	376189	C3D10H	216092
$9 \cdot s$	Shore 30A Silicone	415347	C3D10H	237455

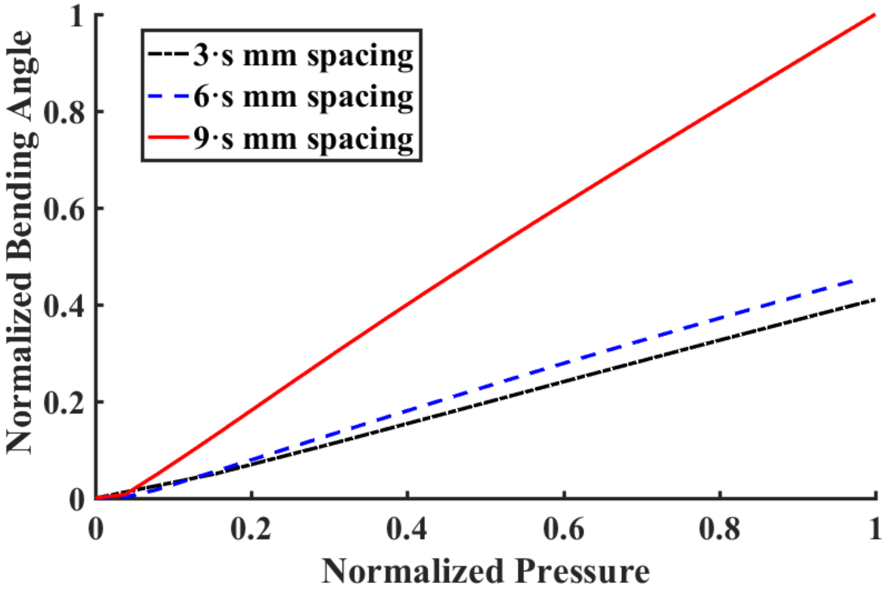

Figure 40: Normalized bending angle vs. normalized pressure plot for actuator spacing of $3 \cdot s\ mm$, $6 \cdot s\ mm$, $9 \cdot s\ mm$.

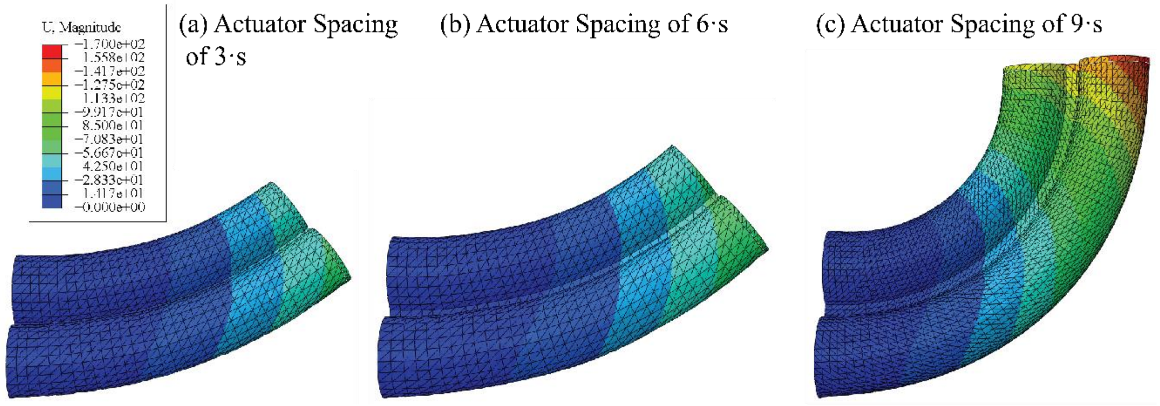

***Figure 41**: Displacement contours of 3CA FEM model for different values of actuator spacing.*

The results obtained from these models are used to plot normalized bending angle vs normalized pressure as shown in figure 40. In fig.40, The red curve shows the normalized bending angle vs. normalized pressure for the 3CA with $9 \cdot s\ mm$ spacing between actuators. The blue curve shows the normalized bending angle vs. normalized pressure for the 3CA with $6 \cdot s\ mm$ spacing between actuators. The black curve shows the normalized bending angle vs normalized pressure for the 3CA with $3 \cdot s\ mm$ spacing between actuators. In fig. 40, 3CA with $9 \cdot s\ mm$ actuator spacing has more extension at same pressure when compared to 3CA with $3 \cdot s\ mm$ actuator spacing and $6 \cdot s\ mm$ actuator spacing. The difference in extension between 3CA with $6 \cdot s\ mm$ actuator spacing and 3CA with $3 \cdot s\ mm$ actuator spacing is 9.426 %. The calculated mass of the 3CA with $9 \cdot s\ mm$ actuator spacing is 7% higher than 3CA with $3 \cdot s\ mm$ actuator spacing and calculated mass of the 3CA with $6 \cdot s\ mm$ actuator spacing is 3.5% higher than 3CA with 3mm actuator spacing. One of the important design requirement is to keep the weight of the arm below 2 kg, hence 3CA with $3 \cdot s\ mm$ actuator spacing over 3CA with $9 \cdot s\ mm$ actuator spacing and 3CA with $6 \cdot s\ mm$ actuator spacing.

Taper ratio

Taper ratio is the ratio of the bottom radius of the RRA of the last segment to the top radius of the RRA of the first segment. It is denoted by 't_r'. To study the effect of taper ratio on the bending angle of 3CA, the sheath is assigned shore 30A silicone material's properties, actuator spacing is set to $3 \cdot s\ mm$, and the RRAs are assigned optimal parameter values as discussed in chapter 5, and all other parameters are varied in the FEM model as shown in table 9.

***Table 9**: Number of nodes and elements of the FEM models used to study the effect of taper ratio.*

Taper Ratio	Actuator Spacing (mm)	Sheath Material	Number of Nodes	Element Type	Number of Elements
0.25	$3 \cdot s$	Shore 30A Silicone	715770	C3D10H	380093
0.375	$3 \cdot s$	Shore 30A Silicone	560731	C3D10H	304347
0.5	$3 \cdot s$	Shore 30A Silicone	739565	C3D10H	445565
0.625	$3 \cdot s$	Shore 30A Silicone	365346	C3D10H	197765
0.75	$3 \cdot s$	Shore 30A Silicone	589111	C3D10H	334728

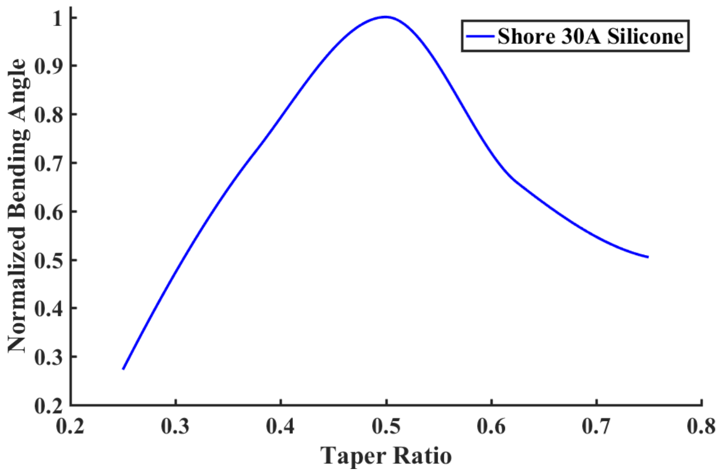

***Figure 42**: Normalized bending angle vs. taper ratio plot of 3CA with silicone sheath of shore hardness 30A.*

(a) Taper ratio of 0.250 (b) Taper ratio of 0.375 (c) Taper ratio of 0.500

(d) Taper ratio of 0.625 (e) Taper ratio of 0.750

***Figure 43**: Displacement contours of 3CA FEM model for different taper ratios.*

The data from simulation results are used to plot normalized blending angle vs taper ratio, as shown in figure 42. The values of taper ratio are taken on x-axis and values of normalized bending angle are taken on the y-axis. As the taper ratio increases from 0.25 to 0.5, the normalized bending angle increases and normalized bending angle drops as the taper ratio is increased from 0.5 to 1. Therefore, taper ratio of 0.5 is chosen as it gives the maximum bending angle. Figure 43 shows the displacement contours for various taper ratios obtained from the results of FEM Model simulations.

Sheath Material

To study the effect of material properties of the sheath on the 3CA, FEM model discussed previously is used. Properties of the materials of the sheath are varied in the FEM models using shore 10A silicone, shore 20A silicone, and shore 30A silicone. Taper ratio of the 3CA is set as 0.5, Actuator spacing of the 3CA is set as $3 \cdot s\ mm$, and all the parameters of individual RRAs are set as mentioned in chapter 5. The number of nodes and elements used to mesh the 3CA in the FEM models are given in table 10.

***Table 10**: Number of nodes and elements of FEM models used to study the effect of the sheath material.*

Actuator Spacing (mm)	Sheath Material	Number of Nodes	Element Type	Number of Elements
$3 \cdot s$	Shore 30A Silicone	739565	C3D10H	445565
$3 \cdot s$	Shore 20A Silicone	739565	C3D10H	445565
$3 \cdot s$	Shore 10A Silicone	739565	C3D10H	445565

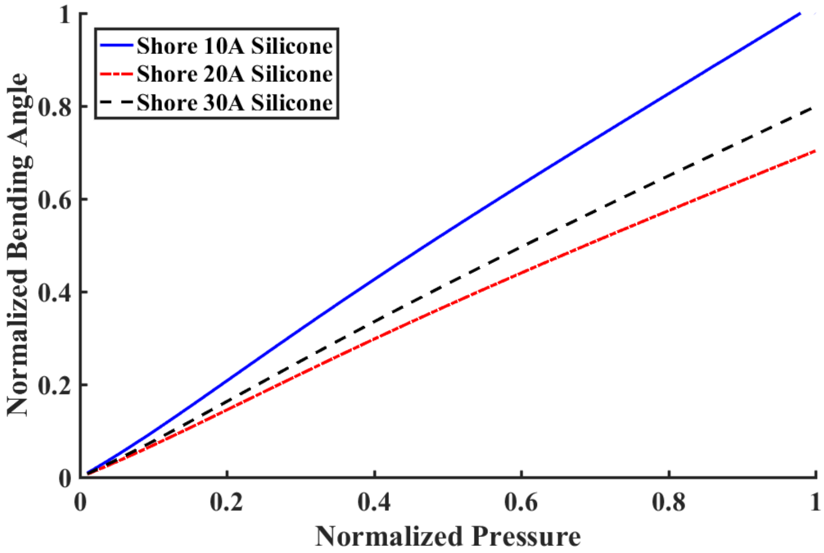

***Figure 44**: Normalized bending vs. normalized pressure plot to study the effect of material properties of 3CA Sheath.*

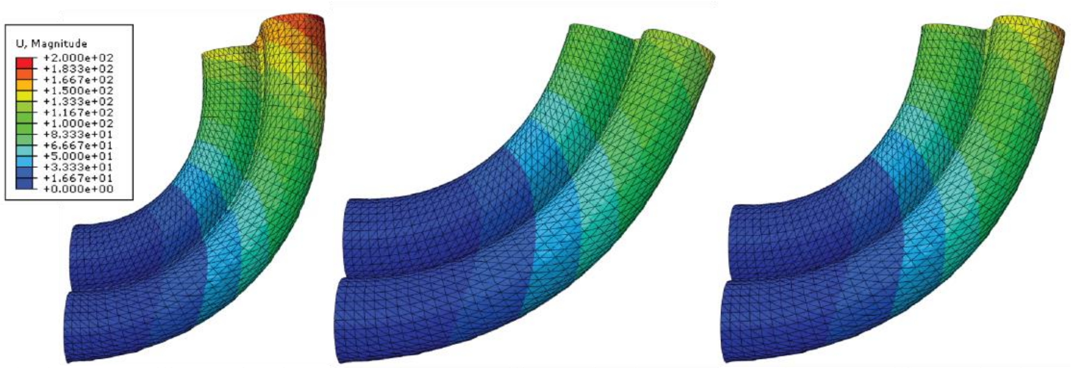

(a) Shore 10A Silicone Sheath (b) Shore 20A Silicone Sheath (c) Shore 30A Silicone Sheath

***Figure 45**: Displacement contours of 3CA FEM model for different sheath materials.*

The results obtained from simulating various models are used to plot normalized bending angle against normalized pressure as shown in figure 44. Figure 45 shows the displacement contours of the FEM models with different sheath materials and the scale shows the magnitude of the displacement in *mm*. The graph in fig. 44 shows that the calculated bending angle is higher for 3CA with shore 10A silicone sheath compared to 3CA with shore 30A silicone sheath and 3CA with shore 20A silicone sheath. The bending angle achieved by 3CA with shore 10A silicone sheath is 42% higher than 3CA with shore 20A silicone sheath, 25% higher than 3CA with shore 30A silicone sheath. The bending angle achieved by 3CA with shore 30A silicone sheath is 13% higher than 3CA with shore 20A silicone sheath. The tensile strength of shore 10A silicone, shore 20A silicone, shore 30A silicone are 475 *psi*, 550 *psi*, 500 *psi* respectively. Further investigations on the FEM model showed that the maximum actuation pressure that the 3CA can hold without failing, with shore 10A silicone sheath is 517.107 *kPa*, shore 20A silicone sheath is 689.47 *kPa*, and shore 30A silicone sheath is 689.47 *kPa*. From design requirements and the results, the best compromise is made between the maximum actuation pressure of 3CA, bending angle of 3CA, the tensile strength of the sheath and shore 30A silicone is chosen as the material for the sheath of 3CA of SPL.

Summary of modeling of 3CA

After performing simulations to study the effect of the actuator spacing, taper ratio and material of the sheath on the bending angle of the 3CA using computational modeling, optimal values for the parameters are selected and tabled in table 11. Actuator spacing of $3 \cdot s\ mm$ is chosen to reduce the overall weight of the 3CA compromising on the bending ability at lower pressures. Taper ratio of 0.5 is chosen as this ratio provides the highest bending angle at same pressure when compared to other ratios. Shore 30A silicone is chosen as the material of the sheath as it has the best combination of the tensile strength and bending angle of 3CA.

***Table 11**: Optimal values for the parameters of 3CA.*

S. No	Parameter	Optimal Value/Material
1	Actuator Spacing	$3 \cdot s\ mm$
2	Taper Ratio	0.5
3	Sheath Material	shore 30A silicone

Fabrication of 3CA

Three-Chambered Actuator (3CA) is fabricated using a two-part mold designed using a CAD software (SolidWorks, Dassault Systemes, FRA) and high spatial resolution 3D printers (Objet350, Stratasys, MN and Fortus450, Stratasys, MN) as shown in figure 37(c). The two-part mold consists of two molds with dowel pin holes and no impressions, designed to bond three RRAs together. The two pieces of the mold are secured together and three uncapped RRAs with the cores are placed in the mold with the help of dowel pins and cores. The silicone mixture of shore 30A silicone is poured into the mold setup and the three RRAs are centered using a cap. The complete setup is now placed in the oven to expedite the curing process. Once cured, the three-chambered actuator is removed from the mold and cores are removed from RRAs. A seal tape is used to cover the outer surface of the 3CA apart from the top and bottom faces. Two parts of silicone namely Part A and Part B are mixed in a ratio mentioned by the manufacturers and the mixture is poured into a shallow container. The bottom face of the 3CA is dipped into the shallow container and allowed it to cure so that the bottom face of the 3CA is capped. The above process is repeated to cap the top face of the 3CA.

Evaluation of 3CA

Bending Angle Test

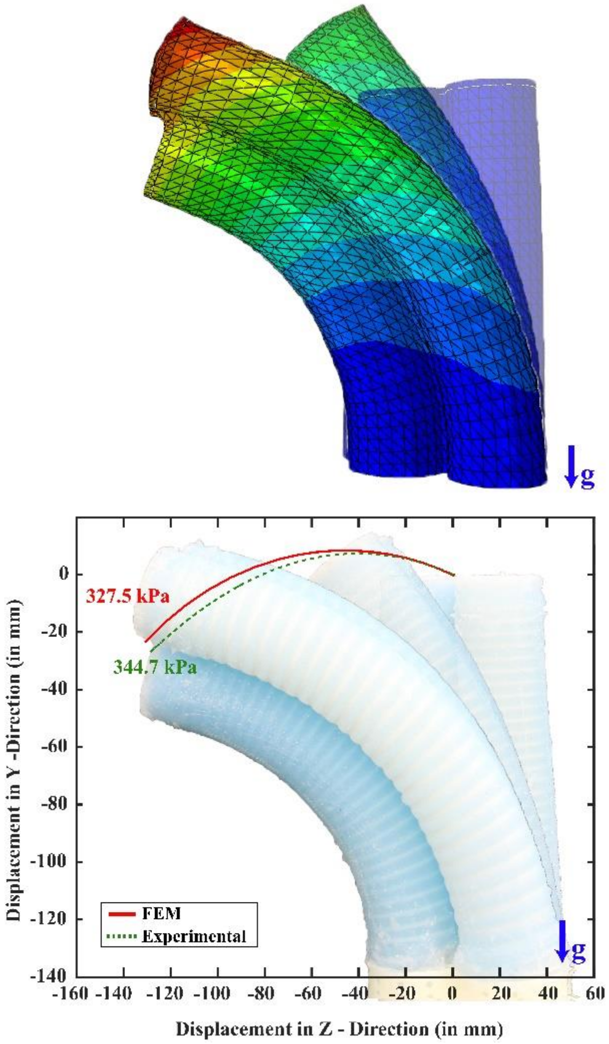

***Figure 46**: Displacement contours of 3CA FEM model when two actuators are pressurized from 0 to 344.7 kPa (top), graph showing the displacement of the bottom face in Y and Z direction and the displacement of 3CA prototype. (bottom)*

To validate the computational models used to study the behavior of three-chambered actuator a bending angle test is performed. In this test, two adjacent RRAs are pressurized quasi-statically from 0 to 344.7 *kPa*. Co-ordinates of the center of the bottom face of 3CA are obtained by using a set of passive reflective markers placed in the center of the bottom face of 3CA and on the circumference of the top face of 3CA to create a ground plane.

Motion capture technology is used to record the coordinates of these reflective markers. The coordinates obtained from the motion capture technology are used to plot coordinates in Y direction against coordinates in the Z direction as shown in figure 46. The position obtained by the bottom end of the actuator in the FEM model reached the desired bending angle (90° in case of SPL) at an actuation pressure of 327.5 kPa, whereas the 3CA in the experiment required an actuation pressure of 344.7 kPa. The maximum pressure error for FEM vs. experimental data is 4.98%. The RMS error of the data for FEM and experimental is 2.7 mm. These results show that the computational model of the 3CA which is described in previous sections can be used to accurately understand the behavior of the 3CA prototype.

CHAPTER 7

SOFT POLY-LIMB

Modeling and Fabrication of SPL

***Figure 47**: Meshed FEM model of SPL.*

A FEM model is constructed, as shown in figure 47, to investigate the ability of a computational model to predict the non-linear behavior of SPL, when actuators of different segments are pressurized to generate a complex pose. Shore 30A silicone material's properties are assigned to the sheath material and the inner tube material of all the segments and properties of digital ABS plastic are assigned to the reinforcement rings in the FEM models. Tie constraints are used to constrain the rings to the outer surface of RRAs, to constrain the sheath to the outer surface of RRA, and to constrain the bottom face of 3CA to top face of next segment 3CA. RRAs, 3CAs of the SPL are meshed using solid tetrahedral quadratic hybrid elements (C3D10H). The number of nodes and elements used to mesh the FEM model are shown in table 12.

***Table 12**: Number of nodes and elements of the FEM model of SPL.*

RRA Material	Sheath Material	Number of Nodes	Element Type	Number of Elements
Dragon Skin 30	Dragon Skin 30	885987	C3D10H	497086

SPL is made of modular 3CA segments as shown in figure 37(e), each of these 3CAs is tapered as per the taper ratio selected. The RRAs are fabricated as discussed in section 5.2, 3CAs are fabricated using the RRAs as discussed in section 6.2. A set of connector pieces are designed, and 3D printed from a digital ABS material, these connector pieces are attached to the top face and bottom face of the 3CA using a silicone adhesive (Sil-Poxy, Smooth-On Inc., PA). The design of these connector pieces allows easy attachment and detachment of the 3CA segments using nuts and bolts. The connector pieces have a small opening in the side through which the fluidic tubing line fitted to the RRAs is routed.

Evaluation of SPL

Arbitrary Pose Test

To investigate the ability of the FEM model to predict the motion of SPL, an arbitrary pose test is performed, where the actuators of FEM model are pressurized to achieve a complex pose and the same pressures are used to actuate the SPL prototype. The SPL prototype is mounted on to a mannequin by attaching it to a backpack. Three passive reflective markers are placed along the circumference of the connector piece of each 3CA segment. A total of 12 markers are used to create rigid bodies at each intersection of two 3CA segments using motion capture technology. Chamber 2 and 3 of the first segment (figure 48) is pressurized to 345 kPa, Chamber 5 and 6 of the second segment are pressurized to 86 kPa and 345 kPa respectively, Chamber 9 is pressured to 59 kPa to achieve an arbitrary complex pose as shown in figure 49.

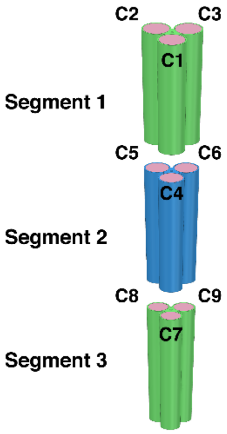

Figure 48*: Exploded view of SPL, showing different segments and chambers.*

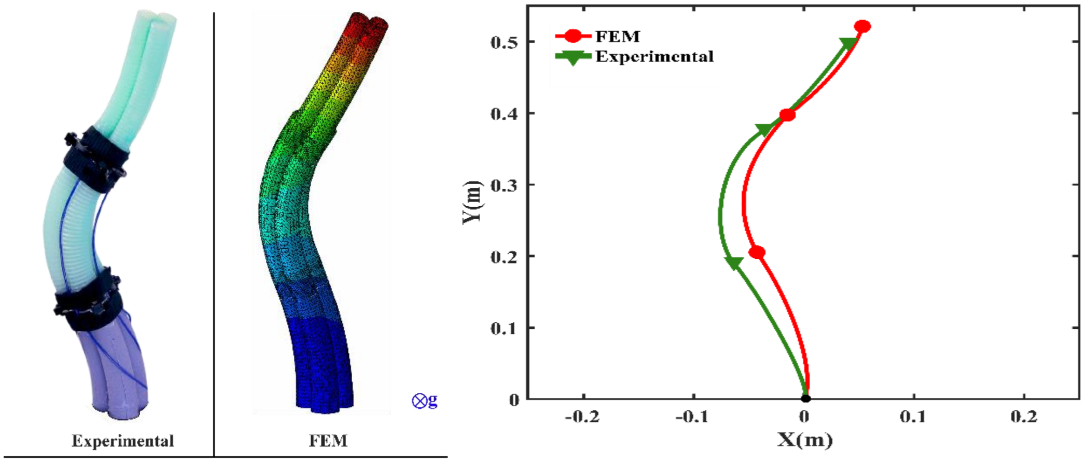

Figure 49*: Arbitrary complex pose achieved by SPL prototype and FEM model (left), graph to compare the data from FEM and SPL prototype (right).*

Motion capture technology is used to extract the coordinates of the SPL from the experiment. The coordinates obtained from FEM and the experiment are used to plot a graph as shown in figure 49. The circle red dots indicate the intersection of segments in FEM and green arrows indicate the rigid bodies in the motion capture experiment. The graph demonstrates that the FEM and experimental results follow a very similar pattern and the Euclidean displacement error is found to be 63.3 *mm*, and a maximum displacement error of 11.45 % is seen when the data is compared.

CHAPTER 8

CONCLUSION AND FUTURE WORK

This thesis identifies different geometrical and physical parameters that can affect the performance of the RRA, 3CA and SPL. The behavior of the RRA, 3CA and SPL when the values of these parameters are varied are studied using a quasi-static computational model. The selected optimal parameters resulted from the analysis of the behavior of RRA are used to fabricate RRA, 3CA and SPL. RRA, Experimental results from Linear Expansion Test of RRA, Bending Angle Test of 3CA and Arbitrary Pose Test of SPL demonstrate the performance of these actuators. FEM models are validated using the experimental results demonstrating that the proposed models can be used to accurately understand the behavior of RRA, 3CA and SPL. The maximum displacement error between the experimental RRA data and RRA FEM model is only 0.54%, the maximum pressure error between the experimental 3CA data and 3CA FEM data is 4.98 % and the maximum displacement error between the experimental SPL data and SPL FEM data is 11.45%. These statistics show that the FEM models very accurately predict the non-linear behavior of these actuators.

***Table 13**: Design requirements and their achieved values of the SPL.*

S. No	Requirement	Requirement Type	Desired Values	Achieved Values
1	Weight	Physical	< 2.0 kg	1.6 kg
2	Length	Physical	0.60 m	0.60 m
3	Actuation Method	Physical	Pneumatic	Pneumatic
4	Tapering of SPL	Physical	Yes	Yes
5	Payload Capacity	Functional	> 0.5 kg	0.3 kg
6	Wearable	Functional	Yes	Yes
7	Durability of RRA	Functional	> 1 million cycles	1,100,000 cycles

After performing various experiments, the achieved values of the design requirements of SPL are compared with the desired values in table 13.

In future, the dynamic behavior of the RRA, 3CA and SPL will be studied. The fabrication process will be improvised to speed up the process of fabricating RRA, 3CA and SPL. The behavior of SPL made out of 3CAs with different sheath material will be investigated in future using FEM models and will be validated by performing experiments. The current prototypes prepared may not be perfect they might be having impurities, comparing experimental results from such prototypes with the results obtained from the computational models may not give accurate results and it might be one of the reasons for errors, which should be investigated. Usage of advanced manufacturing methods such as injection molding will be considered for fabricating the actuators to eliminate the impurities. A tool will be developed to assist the robotic community in which the desired design parameter values are inputted and optimal parameters for the SPL will be given as output.

REFERENCES

Ajiboye, A. B., Willett, F. R., Young, D. R., Memberg, W., Walters, B. C., Sweet, J. A., … Kirsch, R. F. (2017). Restoration of reaching and grasping in a person with tetraplegia through brain-controlled muscle stimulation: a proof-of-concept demonstratio. *The Lancet*, *6736*(17), (In press). https://doi.org/10.1016/S0140-6736(17)30601-3

Ali. (2010). A Review of Constitutive Models for Rubber-Like Materials. *American Journal of Engineering and Applied Sciences*, *3*(1), 232–239. https://doi.org/10.3844/ajeassp.2010.232.239

Bar-Cohen, Y. (2000). Electroactive polymers as artificial muscles - capabilities, potentials, and challenges. *Robotics 2000*, 188–196. https://doi.org/10.1061/40476(299)24

Bishop-Moser, J., Krishnan, G., Kim, C., & Kota, S. (2012). Design of soft robotic actuators using fluid-filled fiber-reinforced elastomeric enclosures in parallel combinations. In *IEEE International Conference on Intelligent Robots and Systems* (pp. 4264–4269). https://doi.org/10.1109/IROS.2012.6385966

Ching-Ping Chou, & Hannaford, B. (1996). Measurement and modeling of McKibben pneumatic artificial muscles. *IEEE Transactions on Robotics and Automation*, *12*(1), 90–102. https://doi.org/10.1109/70.481753

Cianchetti, M., Arienti, A., Follador, M., Mazzolai, B., Dario, P., & Laschi, C. (2011). Design concept and validation of a robotic arm inspired by the octopus. In *Materials Science and Engineering C* (Vol. 31, pp. 1230–1239). https://doi.org/10.1016/j.msec.2010.12.004

Cianchetti, M., Ranzani, T., Gerboni, G., Falco, I. De, Laschi, C., Member, S., & Menciassi, A. (2013). STIFF-FLOP Surgical Manipulator : mechanical design and experimental characterization of the single module, 3576–3581.

Coral, W., Rossi, C., Colorado, J., Lemus, D., & Barrientos, A. (2012). SMA-Based Muscle-Like Actuation in Biologically Inspired Robots : A State of the Art Review. *Smart Actuation and Sensing Systems – Recent Advances and Future Challenges*, 53–82. https://doi.org/10.5772/50209

Deimel, R., & Brock, O. (2013). A compliant hand based on a novel pneumatic actuator. In *Proceedings - IEEE International Conference on Robotics and Automation* (pp. 2047–2053). https://doi.org/10.1109/ICRA.2013.6630851

Doumit, M., Fahim, A., & Munro, M. (2009). Analytical modeling and experimental validation of the braided pneumatic muscle. *IEEE Transactions on Robotics*, *25*(6), 1282–1291. https://doi.org/10.1109/TRO.2009.2032959

Elsayed, Y., Vincensi, A., Lekakou, C., Geng, T., Saaj, C. M., Ranzani, T., … Menciassi, A. (2014). Finite Element Analysis and Design Optimization of a Pneumatically Actuating Silicone Module for Robotic Surgery Applications. *Soft Robotics*, *1*(4), 255–262. https://doi.org/10.1089/soro.2014.0016

Galloway, K. C., Polygerinos, P., Walsh, C. J., & Wood, R. J. (2013). Mechanically programmable bend radius for fiber-reinforced soft actuators. In *2013 16th International Conference on Advanced Robotics, ICAR 2013*. https://doi.org/10.1109/ICAR.2013.6766586

Giorelli, M., Renda, F., Calisti, M., Arienti, A., Ferri, G., & Laschi, C. (2015). Neural Network and Jacobian Method for Solving the Inverse Statics of a Cable-Driven Soft Arm with Nonconstant Curvature. *IEEE Transactions on Robotics*, *31*(4), 823–834. https://doi.org/10.1109/TRO.2015.2428511

Grzesiak, A., Becker, R., & Verl, A. (2011). The Bionic Handling Assistant: a success story of additive manufacturing. *Assembly Automation*, *31*(4), 329–333. https://doi.org/10.1108/01445151111172907

Guterstam, A., Petkova, V. I., & Ehrsson, H. H. (2011). The Illusion of Owning a Third Arm, *6*(2). https://doi.org/10.1371/journal.pone.0017208

Huang, W. (1998). Shape memory alloys and their application to actuators for deployable structures. *Engineering*, 192. Retrieved from http://www.ntu.edu.sg/home/mwmhuang/cambridge/Phd2side.pdf

Ilievski, F., Mazzeo, A. D., Shepherd, R. F., Chen, X., & Whitesides, G. M. (2011). Soft robotics for chemists. *Angewandte Chemie - International Edition, 50*(8), 1890–1895. https://doi.org/10.1002/anie.201006464

Immega, G., Antonelli, K., & Ko, J. (1995). Teleoperation of the KSI Tentacle Manipulator for Hot Cell Decontamination. In *IEEE International Conference on Systems, Man and Cybernetics. Intelligent Systems for the 21st Century* (pp. 2133–2136). https://doi.org/10.1109/ICSMC.1995.538095

Jiang, H., Liu, X., Chen, X., Wang, Z., Jin, Y., & Chen, X. (2016). Design and simulation analysis of a soft manipulator based on honeycomb pneumatic networks. In *2016 IEEE International Conference on Robotics and Biomimetics, ROBIO 2016* (pp. 350–356). https://doi.org/10.1109/ROBIO.2016.7866347

KIER, W. M., & SMITH, K. K. (1985). Tongues, tentacles and trunks: the biomechanics of movement in muscular-hydrostats. *Zoological Journal of the Linnean Society*, *83*(4), 307–324. https://doi.org/10.1111/j.1096-3642.1985.tb01178.x

Kirby, R. S., Wingate, M. S., Van Naarden Braun, K., Doernberg, N. S., Arneson, C. L., Benedict, R. E., … Yeargin-Allsopp, M. (2011). Prevalence and functioning of children with cerebral palsy in four areas of the United States in 2006: A report from the Autism and Developmental Disabilities Monitoring Network. *Research in Developmental Disabilities*, *32*(2), 462–469. https://doi.org/10.1016/j.ridd.2010.12.042

Klute, G. K., Czerniecki, J. M., & Hannaford, B. (1999). McKibben Artificial Muscles : Pneumatic Actuators with Biomechanical Intelligence, 1–6.

Kofod, G. (2001). Dielectric elastomer actuators. *Smart Materials and Structures*, *14*(September), 1210–1216. https://doi.org/10.1088/0964-1726/14/6/014

Lubelski, D., Alvin, M. D., Nesterenko, S., Sundar, S. J., Thompson, N. R., Benzel, E. C., & Mroz, T. E. (2016). Correlation of quality of life and functional outcome measures for cervical spondylotic myelopathy. *Journal of Neurosurgery: Spine*, *24*(3), 483–489. https://doi.org/10.3171/2015.6.SPINE159

Mahl, T., Hildebrandt, A., & Sawodny, O. (2014). A variable curvature continuum kinematics for kinematic control of the bionic handling assistant. *IEEE Transactions on Robotics*, *30*(4), 935–949. https://doi.org/10.1109/TRO.2014.2314777

Marchese, A. D., & Rus, D. (2015). Design, kinematics, and control of a soft spatial fluidic elastomer manipulator. *The International Journal of Robotics Research*, 0278364915587925-. https://doi.org/10.1177/0278364915587925

McMahan, W., Chitrakaran, V., Csencsits, M., Dawson, D., Walker, I. D., Jones, B. A., … Rahn, C. D. (2006). Field trials and testing of the OctArm continuum manipulator. In *Proceedings - IEEE International Conference on Robotics and Automation* (Vol. 2006, pp. 2336–2341). https://doi.org/10.1109/ROBOT.2006.1642051

Moseley, P., Florez, J. M., Sonar, H. A., Agarwal, G., Curtin, W., & Paik, J. (2016). Modeling, Design, and Development of Soft Pneumatic Actuators with Finite Element Method. *Advanced Engineering Materials*, *18*(6), 978–988. https://doi.org/10.1002/adem.201500503

Ogden, R. W. (1997). *Non linear elastic deformations*.

Pelrine, R. (2000). High-Speed Electrically Actuated Elastomers with Strain Greater Than 100%. *Science*, *287*(5454), 836–839. https://doi.org/10.1126/science.287.5454.836

Plagenhoef, S., Gaynor Evans, F., & Abdelnour, T. (1983). Anatomical Data for Analyzing Human Motion. *Research Quarterly for Exercise and Sport*, *54*(2), 169–178. https://doi.org/10.1080/02701367.1983.10605290

Polygerinos, P., Lyne, S., Wang, Z., Nicolini, L. F., Mosadegh, B., Whitesides, G. M., & Walsh, C. J. (2013). Towards a soft pneumatic glove for hand rehabilitation. *IEEE International Conference on Intelligent Robots and Systems*, 1512–1517. https://doi.org/10.1109/IROS.2013.6696549

Polygerinos, P., Wang, Z., Overvelde, J. T. B., Galloway, K. C., Wood, R. J., Bertoldi, K., & Walsh, C. J. (2015). Modeling of Soft Fiber-Reinforced Bending Actuators. *IEEE Transactions on Robotics*, *31*(3), 778–789. https://doi.org/10.1109/TRO.2015.2428504

Sada, M. Al, Khamis, M., & Kato, A. (2017). Challenges and Opportunities of Supernumerary Robotic Limbs.

Samaranayake, B. G. L. T., Preethichandra, D. M. G., Alahakoon, A. M. U. S. K., & Kaneto, K. (2007). Modeling Simulation and Design of Ionic Polymer Metal Composite Soft Actuators. *International Conference on Industrial and Information Systems*, (August), 8–11. https://doi.org/10.1109/ICIINFS.2007.4579221

Samatham, R., Kim, K. J., Dogruer, D., Choi, H. R., Konyo, M., Madden, J. D., … Yamakita, M. (2007). Active polymers: An overview. In *Electroactive Polymers for Robotic Applications: Artificial Muscles and Sensors* (pp. 1–36). https://doi.org/10.1007/978-1-84628-372-7_1

Simaan, N., Taylor, R., & Flint, P. (2004). High Dexterity Snake-like Robotic Slaves for Minimally Invasive Telesurgery of the Upper Airway. *International Conference on Medical Image Computing and Computer-Assisted Intervention (MICCAI '04) , LNCS 3217, LNCS 3217*, 17–24. https://doi.org/10.1007/978-3-540-30136-3_3

Simaan, N., Xu, K., Wei, W., Kapoor, A., Kazanzides, P., Taylor, R., & Flint, P. (2009). Design and Integration of a Telerobotic System for Minimally Invasive Surgery of the Throat. *International Journal of Robotics Research*, *28*(9), 1134–1153. https://doi.org/10.1177/0278364908104278

Trivedi, D., Rahn, C. D., Kier, W. M., & Walker, I. D. (2008). Soft robotics: Biological inspiration, state of the art, and future research. *Applied Bionics and Biomechanics*. https://doi.org/10.1080/11762320802557865

Tsakiris, M., & Carpenter, L. (2010). Hands only illusion : multisensory integration elicits sense of ownership for body parts but not for non-corporeal objects, 343–352. https://doi.org/10.1007/s00221-009-2039-3

Walker, I. D. (2013). Continuous Backbone "Continuum" Robot Manipulators. *ISRN Robotics*, *2013*, 1–19. https://doi.org/10.5402/2013/726506

Walker, I. D., Dawson, D. M., Flash, T., Grasso, F. W., Hanlon, R. T., Hochner, B., …

Zhang, Q. M. (2005). Continuum robot arms inspired by cephalopods. *SPIE Conference on Unmanned Ground Vehicle Technology*, *5804*, 303–314. https://doi.org/10.1117/12.606201

Xu, K., & Simaan, N. (2010). Analytic Formulation for Kinematics, Statics, and Shape Restoration of Multibackbone Continuum Robots Via Elliptic Integrals. *Journal of Mechanisms and Robotics*, *2*(1), 11006. https://doi.org/10.1115/1.4000519

Yeoh, O. H. (1993). Some Forms of the Strain Energy Function for Rubber. *Rubber Chemistry and Technology*, *66*(5), 754–771. https://doi.org/10.5254/1.3538343

APPENDIX A

GEOMETRICAL PARAMETERS AND PERFORMANCE METRICS OF OCTARM

***Table 14**: Design parameters and values of OctArm IV and OctArm V* (McMahan et al., 2006).

	Section #	1	2	3	4
OCTARM IV	Mesh Angle, ϕ	70°	70°	70°	72°
	Outer Radius, r_o	11 *mm*	11 *mm*	11 *mm*	8.5 *mm*
	Thickness, t	2 *mm*	2 *mm*	2 *mm*	2 *mm*
	Length, L_o	200 *mm*	220 *mm*	250 *mm*	320 *mm*
OCTARM V	Mesh Angle, ϕ	70°	70°	70°	N/A
	Outer Radius, r_o	14 *mm*	14 *mm*	11 *mm*	N/A
	Thickness, t	4.7 *mm*	4.7 *mm*	4.7 *mm*	N/A
	Length, L_o	250 *mm*	280 *mm*	300 *mm*	N/A

***Table 15**: Performance Measurements of OctArm IV and OctArm V* (McMahan et al., 2006).

		OCTARM IV				OCTARM V		
Section Number		1	2	3	4	1	2	3
Vertical Load Capacity (*N*)		300	300	140	90	890	N/A	220
Transverse Load Capacity (*N*)	1 channel	60	60	16	16	120	100	70
	2 channels	85	85	20	20	250	130	80
Max. Bending Angle (*deg*)	1 channel	100	100	280	365	90	180	360
	2 channels	90	100	270	380	90	180	360
Maximum Extension (*mm*)		100	110	140	200	141	144	218
Max % Extension		50	50	55	66	59	60	75
Extension Time (*s*) [to max psi *]		0.65	0.68	0.61	0.31	1.4	2.5	1.6
		* to 60 psi				* to 120 psi		

APPENDIX B

ASTM STANDARDS FOR DUMBBELL-SHAPED TEST SPECIMEN

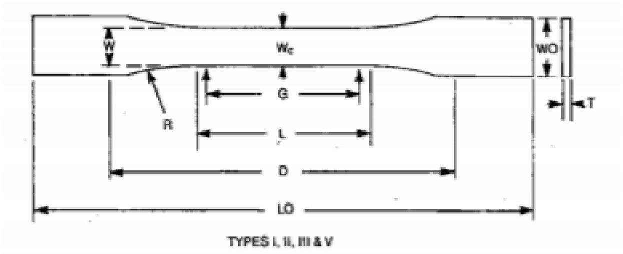

Figure 50*: Dumbbell-shaped test specimen.*

T, Thickness, shall be 3.2± 0.4 mm for all types of molded specimens.

W, Width of narrow section, shall be 3.18±0.5 mm

L, Length of narrow section, shall be 9.53±0.5 mm

WO, Width overall, shall be 9.53±3.18 mm

LO, Length overall, shall be 63.5 mm

G, Gage length, shall be 7.62±0.25 mm

D, Distance between grips, shall be 25.4±5 mm

R, Radius of filet, shall be 12.7±1 mm

The dimensions of the cavity in the mold to prepare the dumbbell-shaped test specimen should be as follows:

W, Width of narrow section, shall be 3.18±0.03 mm

L, Length of narrow section, shall be 9.53±0.08 mm

G, Gage length, shall be 7.62±0.02 mm

R, Radius of filet, shall be 12.7±0.08 mm